Charles University in Prague
Faculty of Science

Department of Physical and Macromolecular Chemistry

New Possibilities in Fluorescence Correlation Spectroscopy

Aleš Benda

Supervisor:
Doc. Dr. Martin Hof

PhD thesis

Prague 2006

The thesis was accomplished at the J. Heyrovský Institute of Physical Chemistry of the Academy of Sciences of the Czech Republic. My supervisor was Doc. Dr. Martin Hof.

I declare that I have elaborated the thesis on my own. If other already published results are used, they are included in the list of references. I agree with lending the thesis to anyone who may be interested.

Prague, 30. 6. 2006

Acknowledgement

My biggest gratitude goes to Martin Hof for his enlightened guidance, for the friendly and fair atmosphere he creates and for giving me the opportunity of scientific and human growth.

I'm also fully indebted to Martin Beneš, Jan Sýkora, Jana Humpolíčková, Adam Miszta, Veronika Faguľová and other colleagues from our lab, who accompanied me during my doctorate studies and with whom I had not only a myriad of fruitful discussions, but also a lot of fun and joy.

Thankful memories are heading towards my international collaborators in Strasbourg, Maastricht, Bordeaux, Wroclaw, Grenoble, Leuven, Halle, Berlin and Jülich. You all make me feel real European. My special thanks are devoted to Wim Hermens and Ralf Richter, whose approach to science and human qualities deserve great respect and whose friendship I really appreciate.

The two people I'm obliged to the most are my parents. Without your care and love I wouldn't be the man I am. Thank you!

My deepest thanks belong to my beloved Katka, who will soon become my wife, for her love, which is my greatest source of inspiration and gives a sense to my life.

List of abbreviations

1D	one-dimensional
1DFCS	one-dimensional fluorescence correlation spectroscopy
2D	two-dimensional
3D	three-dimensional
ACF	autocorrelation function
AFM	atomic force microscopy
BODIPY630	BODIPY® 630/650-X, STP ester
CCD	coupled charge device
CEF	collection efficiency function
CpM	counts per molecule
CR	count rate
cTAR	complementary sequence of the transactivation response region
DIC	differential interference contrast
DiD	1,1′-dioctadecyl-3,3,3′,3′-tetramethylindodicarbocyanine perchlorate
DOPC	Dioleoylphosphatidylcholin
DOPE	Dioleoylphosphatidylethanolamin
DOPS	Dioleoylphosphatidylserin
FCS	fluorescence correlation spectroscopy
FLCS	fluorescence limetime correlation spectroscopy
FLIM	fluorescence lifetime imaging microscopy
FRAP	fluorescence recovery after photobleaching
FRET	fluorescence resonance energy transfer
FWHM	Full width in half maximum
GUVs	giant unilamellar vesicles
HEPES	N-(2-hydroxyethyl)piperazine-N'-(2-ethanesulfonic acid
IRF	instrument response function
ITIES	interface between two immiscible electrolyte solutions
ITO	indium-tin oxide
LUVs	large unilamellar vesicles
MDF	molecular detection function
QCM-D	quartz crystal microbalance with dissipation monitoring
SPBs	supported phospholipid bilayer
SPR	surface plasmon resonance
SUVs	small (sonicated) unilamellar vesicles
TCSPC	time-correlated single photon counting
TIRFM	total internal reflection fluorescence microscopy
TR-FCS	time-resolved fluorescence correlation spectroscopy
TTTR	time-tagged time resolved
VASE	variable angle spectroscopic ellipsometry
VIS	visible

List of publications

First author papers (main frame of the thesis):

Paper I. Benda, A.; Benes, M.; Marecek, V.; Lhotsky, A.; Hermens, W. T.; Hof, M., How to determine diffusion coefficients in planar phospholipid systems by confocal fluorescence correlation spectroscopy. *Langmuir* **2003,** 19, (10), 4120-4126.

Paper II. Benda, A.; Hof, M.; Wahl, M.; Patting, M.; Erdmann, R.; Kapusta, P., TCSPC upgrade of a confocal FCS microscope. *Review of Scientific Instruments* **2005,** 76, (3), 033106.

Paper III. Benda, A.; Fagulova, V.; Deyneka, A.; Enderlein, J.; Hof, M., Fluorescence Lifetime Correlation Spectroscopy combined with Lifetime Tuning: New Perspectives in Supported Phospholipid Bilayer Research. *submitted to Langmuir*

Papers with significant contribution (added to the thesis):

Paper IV. Benes, M.; Billy, D.; Benda, A.; Speijer, H.; Hof, M.; Hermens, W. T., Surface-dependent transitions during self-assembly of phospholipid membranes on mica, silica, and glass. *Langmuir* **2004,** 20, (23), 10129-10137.

Paper V. Humpolickova, J.; Gielen, E.; Benda, A.; Fagulova, V.; Vercammen, J.; VandeVen, M.; Hof, M.; Ameloot, M.; Engelborghs, Y., Probing diffusion laws within cellular membranes by Z-scan fluorescence correlation spectroscopy. *Biophysical Journal, in press*

Paper VI. Przybylo, M.; Sýkora, J.; Humpolíčková, J.; Benda, A.; Zan, A.; Hof, M., The lipid diffusion in giant unilamellar vesicles is more than two times faster than in supported phospolipid bilayers under identical conditions. *submitted to Langmuir*

Papers with significant contribution:

Paper VII. Sheynis, T.; Sykora, J.; Benda, A.; Kolusheva, S.; Hof, M.; Jelinek, R., Bilayer localization of membrane-active peptides studied in biomimetic vesicles by visible and fluorescence spectroscopies. *European Journal of Biochemistry* **2003,** 270, (22), 4478-4487.

Paper VIII. Dertinger, T.; Koberling, F.; Benda, A.; Erdmann, R.; Hof, M.; Enderlein, J., Advanced multifocus confocal laser scanning microscope for single molecule studies. *Proceedings of SPIE* **2005,** 5699, 219-226.

Paper IX. Dertinger, T.; von der Hocht, I.; Benda, A.; Hof, M.; Enderlein, J., Surface sticking and lateral diffusion of lipids in supported bilayers. *submitted to Langmuir*

Paper X. Gielen, E.; Vercammen, J.; Sykora, J.; Humpolickova, J.; vandeVen, M.; Benda, A.; Hellings, N.; Hof, M.; Engelborghs, Y.; Steels, P.; Ameloot, M., Diffusion of sphingomyelin and myelin oligodendrocyte glycoprotein in the membrane of OLN-93 oligodendroglial cells studied by fluorescence correlation spectroscopy. *Comptes Rendus Biologies* **2005,** 328, (12), 1057-1064.

Paper XI. Hohlbein, J.; Steinhart, M.; Schiene-Fischer, C.; Benda, A.; Hof, M.; Hübner, C. G., Confined Diffusion in Ordered Nanoporous Alumina Membranes. *submitted to Nano Letters*

Paper XII. Kral, T.; Benda, A.; Hof, M.; Langner, M., Some aspects of DNA condensation observed by fluorescence correlation spectroscopy. In *Review in Fluorescence 2005*, XXIV ed.; Geddes, C. D.; Lakowicz, J. R., Eds. 2005; Vol. Annual volumes 2005.

Paper XIII. Adjimatera, N.; Benda, A.; Blagbrough, I. S.; Langner, M.; Hof, M.; Kral, T., Fluorescence correlation spectroscopic studies of a single lipopolyamine-DNA nanoparticle. In *Fluorescence of supermolecules, polymers and nanosystems*, Berberan-Santos, M. N., Ed. 2006.

Paper XIV. Adjimatera, N.; Kral, T.; Benda, A.; Hof, M.; Blagbrough, I. S., Understanding the fluorescent signalling behaviour of PicoGreen in lipopolyamines mediated DNA condensation by simultaneous Time-Correlated Single Photon Counting and Fluorescence Correlation Spectroscopy. *In preparation.*

Content

Chapter 1 Introduction

1.1 Objectives and outlines

Fluorescence microscopy is a fast growing branch of optical microscopy, a branch the applications of which lie mainly in the life science research. This work focuses on one special method of fluorescence microscopy, on Fluorescence Correlation Spectroscopy (FCS). The major aim of this work is to develop and demonstrate new possibilities offered by this popular method.

The presented work can be understood from three levels. The first level are the concepts. Firstly, it brings a methodology how to precisely measure diffusion coefficients of labeled species in planar systems using confocal FCS. Secondly, it shows a way for overcoming problems of multiple species analysis using the time-resolved detection. Thirdly, it joins the preceding two concepts and introduces a novel approach how to simultaneously follow and resolve the surface confined and free space diffusion.

The second level is the least visible, but probably the most laborious one. It is about the hidden background of hardware upgrades, improved ways of sample preparation and manipulation, and faster and more robust data analysis including new software algorithms, programs and macros with user friendly interfaces. In other words, the second level are the tools that enable to realize the concepts.

The third level are the applications that arised from the new concepts utilizing the developed tools. The applications reported in this work are mainly from the field of lipid membranes, protein-membrane interactions and DNA condensation.

Chapter 1 gives a brief overview of the main methods and model system used in this thesis. Chapter 2 is based on Paper I, on the "Z-scan" method for precise determination of diffusion coefficients in planar systems, and its various extensions and applications. The hardware and software implementation of Time-Resolved Fluorescence Correlation Spectroscopy (Paper II) together with the resulting applications is described in Chapter 3. The last Chapter 4 is devoted to the fluorescence lifetime tuning within supported phospholipids bilayers, which combined with Time-Resolved Fluorescence Correlation Spectroscopy enables to simultaneously follow and resolve the supported phospholipids bilayers confined and free bulk diffusion (Paper III).

The thesis is based on the results published in the three main publications (Paper I, II, III). This main frame is complemented by the results from the other papers as well as by the yet unpublished data. All the results are briefly introduced and placed into the context of the whole thesis, only the unpublished data are treated in more details.

By showing the new possibilities in fluorescence correlation microscopy and by bringing the newest technological development into a routine daily use this thesis is just the beginning. It gives the tools, explains how to use them, shows the examples of the use, and hopes that many more will soon appear...

1.2 Fluorescence Correlation Spectroscopy (FCS)

1.2.1 Basic principles of FCS

Fluorescence correlation spectroscopy is based on the statistical analysis of the temporal evolution of fluorescence intensity fluctuations coming from a very small detection volume. The correlation analysis provides information on processes that gave rise to these fluctuations.

For the first time, FCS was introduced, experimentally realized and theoretically investigated in 1972-1974 by Elson and Magde[1-3]. Since that time it's widely used for measurements of translational diffusion, rotational diffusion[4], chemical kinetics[5, 6], photon antibunching[7, 8], molecular interactions[9] and conformational fluctuations[10, 11]. Recent technical modifications, like two-photon excitation[12], dual-color cross-correlation FCS[13] and time-resolved FCS[14], largely enhanced measurement and analysis capabilities of standard confocal FCS.

1.2.2 Experimental setup

In 1993 Rigler[15] introduced a confocal FCS setup for measurements with low background and high signal to noise ratio. This setup became the basis not only for first commercial FCS instruments (as is our Confocor 1), but also for majority of nowadays FCS apparatuses.

The used scheme is depicted in Figure 1. The basic part is an inverted epifluorescence confocal microscope. An appropriately attenuated and spectrally cleaned up laser beam is sent through a single-mode optical fiber for mode cleaning. After exiting the fiber, the light is re-collimated, reflected by a dichroic mirror and

focused by a water- or oil- immersion objective into a diffraction limited spot. The emitted fluorescence light is collected by the same objective, passes the dichroic mirror, is spectrally filtered by emission filter and focused by tube lenses onto a pinhole, which spatially filters out light originating out of the focal plane. The passed light is then focused onto the sensitive area of a single-photon counting detector. The electric pulses produced by the detector are fed into a hardware correlator board that online calculates the correlation function and stores it on the hard disk.

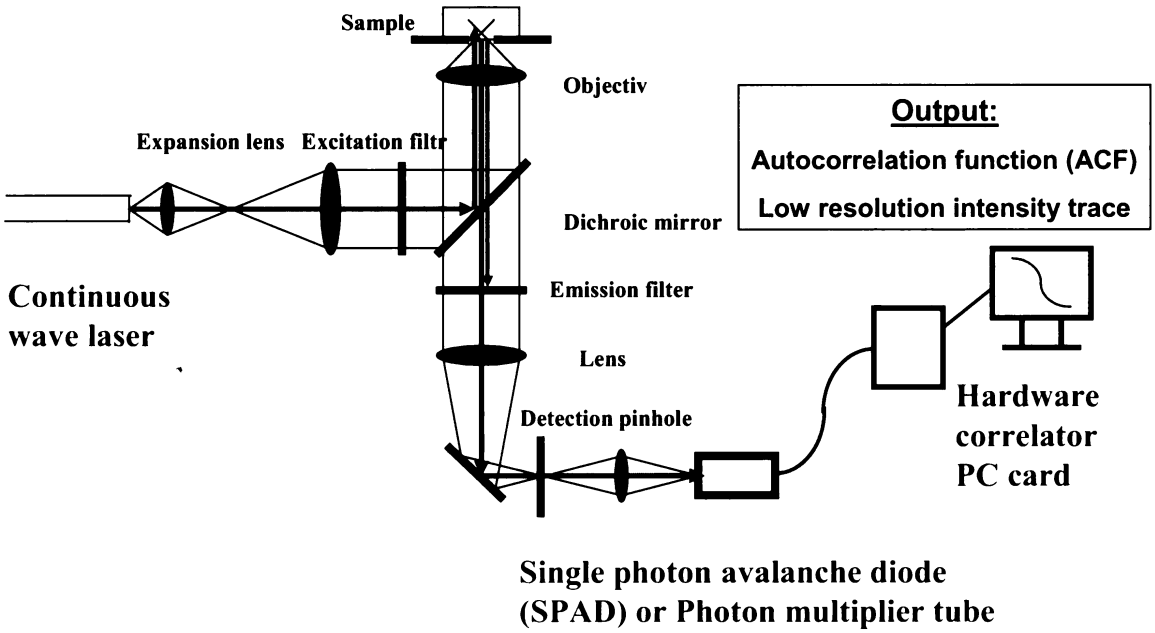

Figure 1. Scheme of the classic FCS setup

1.2.3 Theoretical principles of FCS

The temporal evolution of fluorescence intensity is analyzed by means of the first order autocorrelation function (ACF) $G(\tau)$:

$$G(\tau) = \langle F(t) * F(t+\tau) \rangle \tag{1}$$

where the triangular brackets indicate time averaging, $F(t)$ is the fluorescence signal as a function of time t, and τ is the delay (lag) time.

The definition can be extended into a form containing terms determined by the experimental setup (shown is a form for system containing one type of fluorescent molecules)[16]:

$$G(t) = q^2 \iiint_{-\infty}^{+\infty} I(\mathbf{r},z)\mathrm{CEF}(\mathbf{r},z)\langle \delta c(\mathbf{r},z,0)\delta c(\mathbf{r}^0,z^0,t)\rangle \times I(\mathbf{r}^0,z^0)\mathrm{CEF}(\mathbf{r}^0,z^0)\,d\mathbf{r}\,dz\,d\mathbf{r}^0\,dz^0 \tag{2}$$

where q is a brightness constant given by a product of chromophore's absorption cross-section, quantum yield, and setup detection efficiency, $\mathbf{r}=(x,y)$ is a vector perpendicular to optical z-axes, $I(\mathbf{r},z)$ is excitation intensity at point $(\mathbf{r},z)$, CEF$(\mathbf{r},z)$ is collection efficiency function and $\delta c(\mathbf{r},z,t)$ is fluctuation of fluorophore's concentration at point $(\mathbf{r},z)$ and time t from equilibrium value.

The intensity profile of a focused laser beam $I(\mathbf{r},z)$ can be satisfactorily approximated by the scalar approximation of a Gaussian laser beam[17], resulting in a z-symmetric Gaussian-Lorentzian distribution[18](Figure 2):

$$I(\mathbf{r},z) = I_0(z)\exp\left[-\frac{2r^2}{\omega^2(z)}\right] \quad \text{(Gaussian)} \tag{3}$$

$$\omega^2(z) = \omega_0^2 + \left(\frac{\lambda}{n\pi\omega_0}\right)^2 z^2 \quad \text{(Lorentzian)} \tag{4}$$

$$I_0(z) = \frac{\omega_0^2 I_0}{\omega^2(z)} \tag{5}$$

where I_0 is the excitation intensity in the middle of the laser beam, ω_0 is radius of the laser beam in the focal plane defined as the distance where the intensity drops by $1/e^2$, λ is wavelength of the excitation light in vacuum and n is the refractive index of the medium.

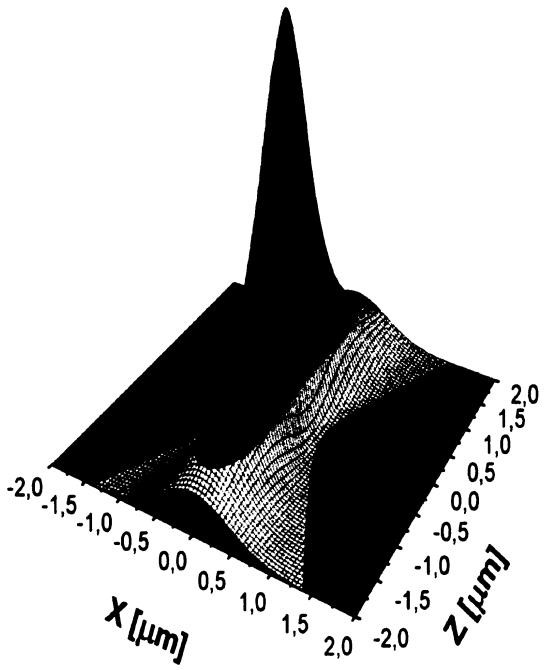

Figure 2. Gaussian-Lorentzian excitation intensity profile in the xz-plane. Red color indicates intensity higher than $1/e^2$ of the maximum intensity in the middle of the focus.

CEF(**r**,*z*) describing the spatial distribution of the detection efficiency of the emitted light can be very precisely calculated using a semigeometrical optical approach[19]. The detection efficiency depends on the wavelength of the emitted light, magnification of the optics, numerical aperture of the objective and size of the pinhole. A crucial part is the pinhole that spatially blocks out-of-focus light. In practice the whole optical system is aligned in such a way that the molecular detection function MDF(**r**,*z*) = I(**r**,*z*)CEF(**r**,*z*) can be approximated by 3-dimensional Gaussian giving an ellipsoidal detection volume[16]. The advantage of this approximation is that the integral in Equation 2 can be solved analytically giving a closed form formula. Although this approximation is very rough[20], for relative measurements it is fully justified.

Taking into account only the translational diffusion, the time averaged concentration autocorrelation term is denoted by Green's function for the diffusion equation in free space[21]:

$$\left\langle \delta c(\mathbf{r},z,0)\delta c(\mathbf{r}^0,z^0,t)\right\rangle = \langle c\rangle \frac{1}{(4\pi Dt)^{3/2}} \exp\left[-\frac{(\mathbf{r}-\mathbf{r}^0)^2+(z-z^0)^2}{4Dt}\right] \qquad (6)$$

Inserting Equation 6 into Equation 2, performing the integration over space for the detection volume described by 3-dimensional Gaussian and performing intensity normalization of the correlation function, one gets the standard equation for free 3-dimensional translational diffusion:

$$G(t) = 1 + \frac{1}{N}\cdot\frac{1}{1+(t/\tau_D)}\left\{\frac{1}{1+(t/\tau_D)SP^{-2}}\right\}^{1/2} \qquad (7)$$

where N is a number of particles in the effective volume V_{eff}, SP is a structure parameter, a constant for the given experimental setup, defined as the ratio of long and short axis of the ellipsoidal detection volume $SP = z_0/\omega_0$, τ_D is diffusion time. The size of the effective volume is[13] $V_{eff} = \pi^{3/2}\omega_0^2 z_0$.

Under the used laser intensities, the photophysics of the used dyes has often an influence on the shape of the ACF. The most often observed phenomenon is intersystem crossing into a triplet state. If the dye molecule is in the long lived triplet state, it is for a certain time invisible. The change from a bright to a dark state and back thus brings a new source of intensity fluctuations, adding another term into the ACF[22]:

$$G(\tau) = 1 + \frac{1}{N\cdot[1-T]}\cdot\left[1 - T\cdot(1-e^{-\tau/t_0})\right]\cdot\frac{1}{1+(\tau/\tau_D)}\cdot\frac{1}{\sqrt{1+SP^{-2}\cdot(\tau/\tau_D)}} \qquad (8)$$

where T is a fraction of the fluorophore in the triplet state and t_0 is relaxation time of the intersystem crossing.

If several noninteracting fluorescence species contribute to the fluorescence signal, the expression in Equation 7 is generalized as follows[23]:

$$G(\tau) = 1 + \frac{\sum_{i=1}^{R} \alpha_i^2 \langle N_i \rangle g_{3di}(\tau)}{\left[\sum_{i=1}^{R} \alpha_i \langle N_i \rangle\right]^2} \tag{9}$$

where $g_{3dim}(\tau) = \left(1 + \frac{\tau}{\tau_{Di}}\right)^{-1} \left(1 + \frac{\tau}{SP^2 \tau_{Di}}\right)^{-1/2}$ and α_i is the experimental brightness of i-th species.

In the case of two-dimensional diffusion the approximation of the molecular detection function by 3-dimensional Gaussian is not acceptable anymore. The illuminated area of the planar sample depends on the relative position of the sample and the laser beam. If the sample is parallel with and close to the focal plane, the effect of the pinhole is small and the MDF is mainly dependant on the excitation intensity profile $I(\mathbf{r},z)$, resulting in two-dimensional Gaussian MDF with radius dependant on the distance from the focal plane. The autocorrelation function for 2D diffusion of one type of fluorescent particles through two-dimensional Gaussian MDF, including the triplet state dynamics, is:

$$G(\tau) = 1 + \frac{1}{N \cdot [1 - T]} \cdot \left[1 - T \cdot (1 - e^{-\tau / t_0})\right] \cdot \frac{1}{1 + (\tau / \tau_D)} \tag{10}$$

The radius of the illuminated area depends on the distance Δz between the sample and the focal plane and is determined by the Lorentzian term of the excitation intensity profile $I(\mathrm{r},z)$ (Equation 4). The ACF fit parameters diffusion time τ_D and particle number N thus also depend on the distance $\Delta z = z - z_0$ between the sample position z and the focal plane position z_0[16, 18]:

$$\tau_D = \frac{\omega_0^2}{4D}\left(1 + \frac{\lambda_0^2 \Delta z^2}{\pi^2 n^2 \omega_0^4}\right) \tag{11}$$

$$N = \pi c \omega_0^2 \left(1 + \frac{\lambda_0^2 \Delta z^2}{\pi^2 n^2 \omega_0^4}\right) \tag{12}$$

where λ_0 is the wavelength of the excitation light in vacuum, n is the refractive index of the environment, D is diffusion coefficient of the fluorescent molecules and c is area concentration of the fluorescent molecules.

1.2.4 Basic information provided by FCS

The autocorrelation curve properly fitted with a suitable model provides valuable information about the studied system. The ACF fit parameters particle number N and diffusion time τ_D are directly related to macroscopic quantities concentration c and diffusion coefficient D. The concentration c is related with particle number N via:

$$c = \frac{N}{N_A V_{eff}} \tag{13}$$

where N_A is Avogadro constant and V_{eff} is effective volume, for 3D Gaussian approximation equal to $V_{eff} = \pi^{3/2} \omega_0^2 z_0$.

The relation between the diffusion coefficient D and the diffusion time τ_D is:

$$D = \frac{\omega_0^2}{4\tau_D} \tag{14}$$

The size of the detection volume described by its radius ω_0 and structure parameter SP is experimentally determined by evaluating ACF for a fluorophore with a priori known diffusion coefficient.

The Stokes-Einstein equation for spherical molecules describes the relation of the diffusion coefficient D with the hydrodynamic radii r_h of the fluorescent molecule:

$$r_h = \frac{k_B T}{6 \pi D \eta} \tag{15}$$

where k_B is Boltzman constant, T is thermodynamic temperature and η is viscosity coefficient.

1.3 Time-Resolved Fluorescence Correlation Spectroscopy (TR-FCS)

1.3.1 Introduction

The combination of Time-Correlated Single Photon Counting (TCSPC) and Fluorescence Correlation Spectroscopy (FCS), called Time-Resolved Fluorescence Correlation Spectroscopy (TR-FCS) or Fluorescence Lifetime Correlation Spectroscopy (FLCS), is a method that uses picosecond time-resolved detection for *separating* different ACF contributions. The emphasis is on the word *separating*. TR-FCS does not involve fitting of a multiple-parameter model to a complex autocorrelation function. Instead, a separated autocorrelation function is calculated for each fluorescence lifetime

component, emitted for example by various species in the sample. The only assumption is that the various components have distinct and non-changing lifetime signatures. The core of the method is a statistical separation of different fluorescence contributions on a single photon level.

An essential requirement for TR-FCS is a sub-nanosecond pulsed excitation instead of continuous wave (cw) illumination. The second requirement is the ability to simultaneously measure the fluorescence photon arrival time on two different time scales: relative to the excitation pulse with picosecond resolution (TCSPC) and relative to the start of the experiment with nanosecond precision, in the so-called Time-Tagged Time Resolved (TTTR) data acquisition mode (Figure 3).

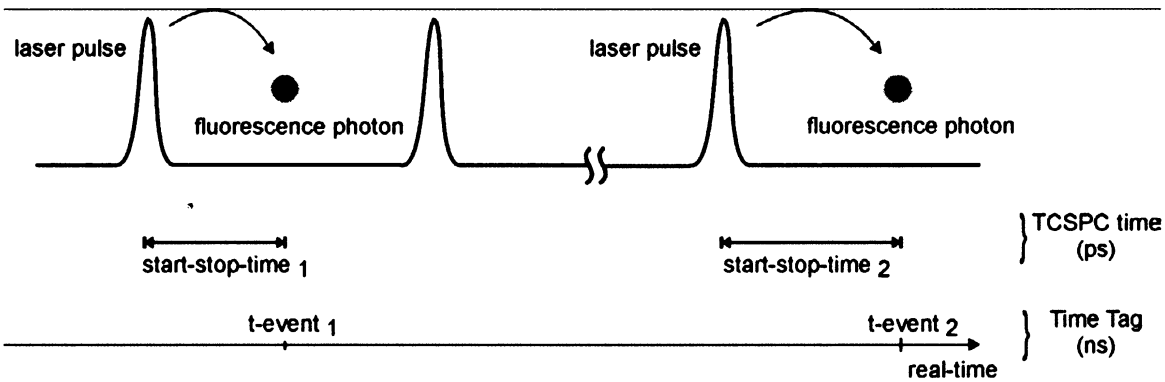

Figure 3. Princip of Time-Tagged Time Resolved data acquisition

The experimental and analysis technique outlined is an important extension of standard FCS. The core idea was published in 2002 by Böhmer and Enderlein[14], but received only little attention until now, although recent publications[24, Paper II, Paper III] present exciting new applications of this method.

1.3.2 Principle

The best way how to explain TR-FCS is to compare TR-FCS with conventional FCS using cw excitation and single channel detection. The standard result of an FCS experiment, the autocorrelation function, is calculated as the two-photon correlation of photon pairs with varying lag-time (Equation 1). This can be done by a hardware autocorrelator, but the recent state-of-the-art is to use more versatile software processing of recorded individual photon arrival times. The core problem of FCS is that if the detected signal contains more than one component, the resulting ACF is a linear combination of the contributions from the different components (Equation 9). A trivial example is a sample with two kinds of diffusing fluorophores, both contributing to the

detected intensity fluctuations. Taking into account the ubiquitous triplet dynamics, scattered excitation light, impurity fluorescence etc., the analysis of the resulting ACF becomes challenging due to the number and mutual influence of adjustable parameters in the model equation used for fitting. In such a case resolving the ACF is difficult[25].

In TTTR data acquisition (Figure 3), the excitation is pulsed and two independent timings are performed for every detected photon event. The macroscopic arrival time measured with respect to the start of the experiment on a continuous time axis contains information related to e. g. translational motion, triplet lifetime etc., and is used just like in conventional FCS. The microscopic delay time measured relative to the excitation pulses contains information about the fluorescence decay on a pico- and nanosecond timescale. It is the simultaneous availability of these two independent timings that makes it possible to calculate separate ACFs for the selected lifetime component.

Let us consider a sample with two fluorescent components, A and B, which have different fluorescence decay kinetics. After each excitation pulse, the photon detection probability decays on a microscopic time scale as shown in Figure 4. The measured decay histogram is a superposition of contributions from A and B, but if the decay characteristics of both components are known a priori, the relative contributions of each component can be extracted by deconvolving the measured histogram. TR-FCS uses this ability to separate contributions based on their lifetime signature, a feature impossible when using cw excitation.

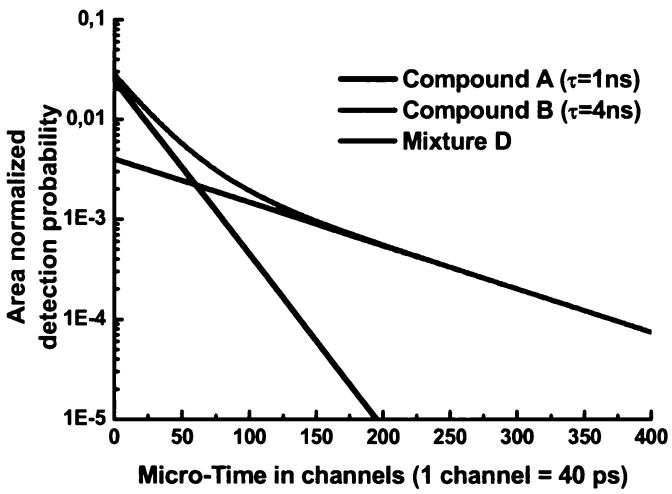

Figure 4. A hypothetical TCSPC histogram of a two-component mixture, $D(i)$ (green line), and its component decays, $A(i)$ (black line) and $B(i)$ (red line). The histogram $D(i)$ is readily available after any TTTR measurement, while the shape of $A(i)$ and $B(i)$ can be obtained from independent TTTR measurements or from the analysis (e. g. fitting) of $D(i)$.

In the TTTR data acquisition, the microscopic delay time is binned into N channels indexed by their number i, so that $i = 1..N$. The maximum number of channels is 4096 for the TimeHarp 200 card, the number of used channels is determined by the laser repetition rate and the channel time width. By histogramming the frequency of various channel numbers encountered and neglecting their macroscopic arrival times one gets the conventional TCSPC decay curve $D(i)$. Next, we will explain how to use the TCSPC information for calculating lifetime-specific ACFs. Let us assume that the TCSPC histograms of the pure components are known (e.g. from a priori measurements on pure samples, or from decay curve analysis) and are denoted by $A(i)$ and $B(i)$. Let us normalize $A(i)$ and $B(i)$ as $a(i)=A(i)/\Sigma A(i)$, $b(i)=B(i)/\Sigma B(i)$, so that $\Sigma a(i)=\Sigma b(i)=1$. We will refer to these normalized curves as decay patterns. The experimentally obtained decay curve of a mixture, $D(i)$, can then be expressed as the linear combination:

$$D(i) = w_a a(i) + w_b b(i) \tag{16}$$

where w_a and w_b are the numbers of photons stemming from compound A and B, respectively. Let us now define two filter functions, $f_a(i)$ and $f_b(i)$, with the following property:

$$\left\langle \sum f_a(i) D(i) \right\rangle = w_a \qquad \left\langle \sum f_b(i) D(i) \right\rangle = w_b \tag{17}$$

where the triangular brackets denote averaging over an infinite number of measurements. In addition, let $f_a(i)$ and $f_b(i)$ minimize the relative errors expressed as:

$$\left\langle \left(\sum f_a(i) D(i) - w_a \right)^2 \right\rangle \qquad \left\langle \left(\sum f_b(i) D(i) - w_b \right)^2 \right\rangle \tag{18}$$

As can be seen from the above expressions, the $f_a(i)$ and $f_b(i)$ act indeed like statistical filters or weighting functions applied to the total decay histogram. They recover the number of photons contributed by each decay component.

Such filters can be numerically calculated from $D(i)$ and from the decay patterns $a(i)$ and $b(i)$ with simple matrix calculations[14]. To simplify the notation we introduce the abbreviations $\mathbf{a}=a(i)$, $\mathbf{b}=b(i)$, $\mathbf{f}_a=f_a(i)$ and $\mathbf{f}_b=f_b(i)$. The decay patterns and filter functions are thus understood to be row vectors of length N. It was shown in previous work[14, 24, 26] that, if the photon counting data obey a Poissonian statistics (which is usually the case for photon counting data), the two filter functions which fulfil the requirements of Equation 17 and Equation 18 can be calculated as:

$$\begin{vmatrix} \mathbf{f}_a \\ \mathbf{f}_b \end{vmatrix} = \left(\begin{vmatrix} \mathbf{a} \\ \mathbf{b} \end{vmatrix} \cdot \mathbf{D} \cdot \begin{vmatrix} \mathbf{a} \\ \mathbf{b} \end{vmatrix}^{\mathrm{T}} \right)^{-1} \cdot \begin{vmatrix} \mathbf{a} \\ \mathbf{b} \end{vmatrix} \cdot \mathbf{D} \tag{19}$$

where the dot · , superscript T and -1 denote matrix multiplication, transposition and inversion, respectively. **D** is a diagonal $N \times N$ matrix constructed from the reciprocal values of counts in the histogram $D(i)$:

$$\mathbf{D} = \begin{vmatrix} \frac{1}{D(1)} & 0 & \cdots & 0 \\ 0 & \frac{1}{D(2)} & \cdots & 0 \\ \vdots & \vdots & \ddots & \vdots \\ 0 & 0 & \cdots & \frac{1}{D(N)} \end{vmatrix} \tag{20}$$

All involved calculations are standard matrix manipulations. Note that in Equation 19 the two filters are calculated together, involving only one matrix inversion. This is essential in order to fulfil the simultaneous requirements of Equation 17 and Equation 18. In contrast, if the $f_a(i)$ and $f_b(i)$ would be calculated separately as $\mathbf{f}_a=(\mathbf{a}\cdot\mathbf{D}\cdot\mathbf{a}^T)^{-1}\cdot\mathbf{a}\cdot\mathbf{D}$ and $\mathbf{f}_b=(\mathbf{b}\cdot\mathbf{D}\cdot\mathbf{b}^T)^{-1}\cdot\mathbf{b}\cdot\mathbf{D}$, they would be useless. Equation 19 is a special case of a more general formula for an arbitrary number x of components:

$$\begin{vmatrix} \mathbf{f}_a \\ \mathbf{f}_b \\ \vdots \\ \mathbf{f}_x \end{vmatrix} = \left(\begin{vmatrix} \mathbf{a} \\ \mathbf{b} \\ \vdots \\ \mathbf{x} \end{vmatrix} \cdot \mathbf{D} \cdot \begin{vmatrix} \mathbf{a} \\ \mathbf{b} \\ \vdots \\ \mathbf{x} \end{vmatrix}^T \right)^{-1} \cdot \begin{vmatrix} \mathbf{a} \\ \mathbf{b} \\ \vdots \\ \mathbf{x} \end{vmatrix} \cdot \mathbf{D} \tag{21}$$

An important feature of the derived filters is their ortonormality with patterns:

$$\mathbf{f}_x \cdot \mathbf{p}_y = \begin{cases} 1, & x = y \\ 0, & x \neq y \end{cases} \tag{22}$$

The ortonormality condition together with the inherent averaging ensures that when the filter for a given lifetime component is applied during the autocorrelation function calculation; a pure ACF for the given component $G_a(\tau)$ is obtained:

$$G_a(\tau) = \langle (\mathbf{f}_a \mathbf{F}(t))(\mathbf{f}_a \mathbf{F}(t+\tau)) \rangle_t = \langle w_a(t) w_a(t+\tau) \rangle_t = \langle F_a(t) F_a(t+\tau) \rangle_t \tag{23}$$

where $\mathbf{F}(t)$ is the overall fluorescence intensity at time t expressed in the form of histogram, w_a is number of photons emitted by compound A at time t, equal to fluorescence intensity $F_a(t)$ of the compound A at time t.

It is valuable to have a look at the shape of $f_a(i)$ and $f_b(i)$ calculated for our hypothetical example. The filters corresponding to the decays depicted in Figure 4 are plotted in Figure 5.

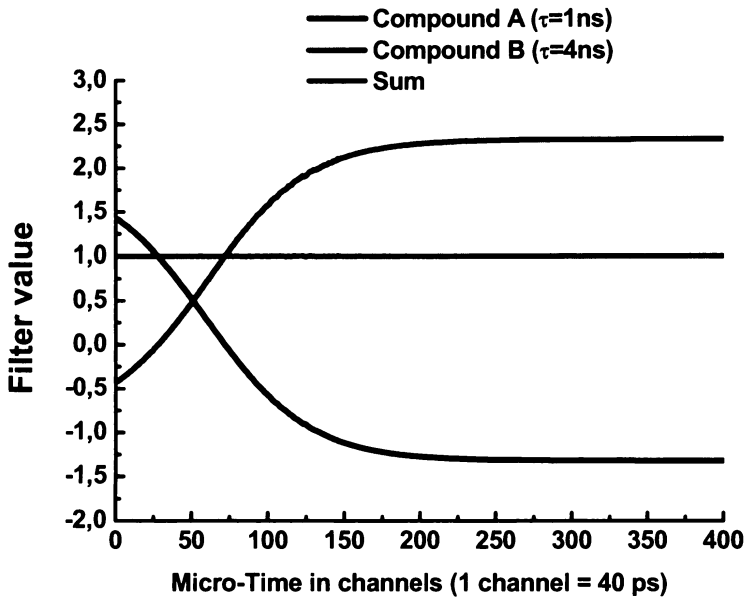

Figure 5. Filter functions ('weights') calculated from $D(i)$, $A(i)$ and $B(i)$ according to Equation 19.

The key point is that using $f_a(i)$ and $f_b(i)$ makes possible to statistically separate the intensity contributions of A and B, photon by photon. In other words, the sign and magnitude of a single photon contribution to the autocorrelation can be determined from the photon's channel number using the corresponding filter function.

When correlating the photon records by a conventional FCS approach, every photon contributes equally and the calculation involves only zeros and ones. In TR-FCS, the filter value corresponding to the photon's channel number is used instead. The numbers entering the ACF calculation are therefore not integers, their absolute value can exceed one, and their sign can even be negative! However note that the sum of the filter values corresponding to a given channel number is always one.

Any physical interpretation of filter values can be misleading and we do not recommend these attempts. The weighting is statistical in principle; therefore the only meaningful results are obtained if the data are satisfactorily averaged. The more photons one has, the better is the accuracy of the resulting separated ACFs. Typical FCS measurements collect more than 10^6 photons and the ACF separation works reliably[14, 24, Paper II, Paper III]. Of course, this also depends on how large the difference between the decay patterns is. Practical experience shows that a factor two difference in lifetimes is sufficient.

1.4 Ellipsometry

1.4.1 Introduction

Ellipsometry is a very sensitive non-destructive optical technique for the characterization and observation of events at an interface or film between two media. It is based on exploiting the polarization transformation that occurs as a beam of polarized light is reflected from a surface or a film. It derives its sensitivity from the determination of the relative phase change in a beam of reflected polarized light. Although known for almost a century, the use of ellipsometry has increased rapidly in the recent years, as novel and automated instrumentation and technique for error-free data analysis were developed.

Ellipsometry is a convenient and accurate technique for the measurement of thicknesses and refractive indexes of very thin films on solid surfaces and for the measurement of optical constants of reflecting surfaces. The lower limit of film thicknesses that can be studied by ellipsometry are on the order of Angstroms.

Most of the nowadays applications involve measurements of optical properties of surfaces and thin films in the air or in vacuum using the variable angle spectroscopic ellipsometry (VASE) for reaching the highest precision. Moreover another advantage of ellipsometry is its adaptability for studying thin films under liquids, a feature we exploit the most.

1.4.2 Principle

The use of ellipsometry for studying thin organic films under water is a rather specialized topic compared to the standard use of ellipsometry in semiconductor science. The experimental setup is more complicated, as a cuvette with immersion liquid (buffer) is introduced into the optical path. This fact together with the insensitivity of refractive index of organic compounds on the wavelength of the light hugely limits the use of VASE. On the other hand, kinetics of surface related processes is often accessed thus requiring fast data acquisition, ideally down to milliseconds resolution.

First ellipsometry measurements on protein absorption to surfaces was carried out already in 1942 by Rothen[27], first measurement on supported lipid membranes and

subsequent protein absorption were performed in the eighties by the group of Hermens[28, 29].

For measurements in liquids a simple one-angle one-wavelength ellipsometer working in null or rotating analyzer mode is mostly used. The scheme is depicted in Figure 6. The relative phase change in a beam of reflected polarized light can be characterized by two values, represented by the ellipsometry readings called azimuthal angle Δ and relative phase shift Ψ. In null mode the ellipsometry angles are directly related to the physical angle of polarizer P and analyzer A, which are set into such positions, that the intensity of the passed light is minimum, ideally null. In rotating analyzer mode the analyzer is fast rotating and the intensity of the passed light is recorded. The resulting intensity time trace is harmonic function carrying information about the polarization state of the reflected beam. By comparison to the initial polarization state, ellipsometry readings Δ and Ψ are recovered.

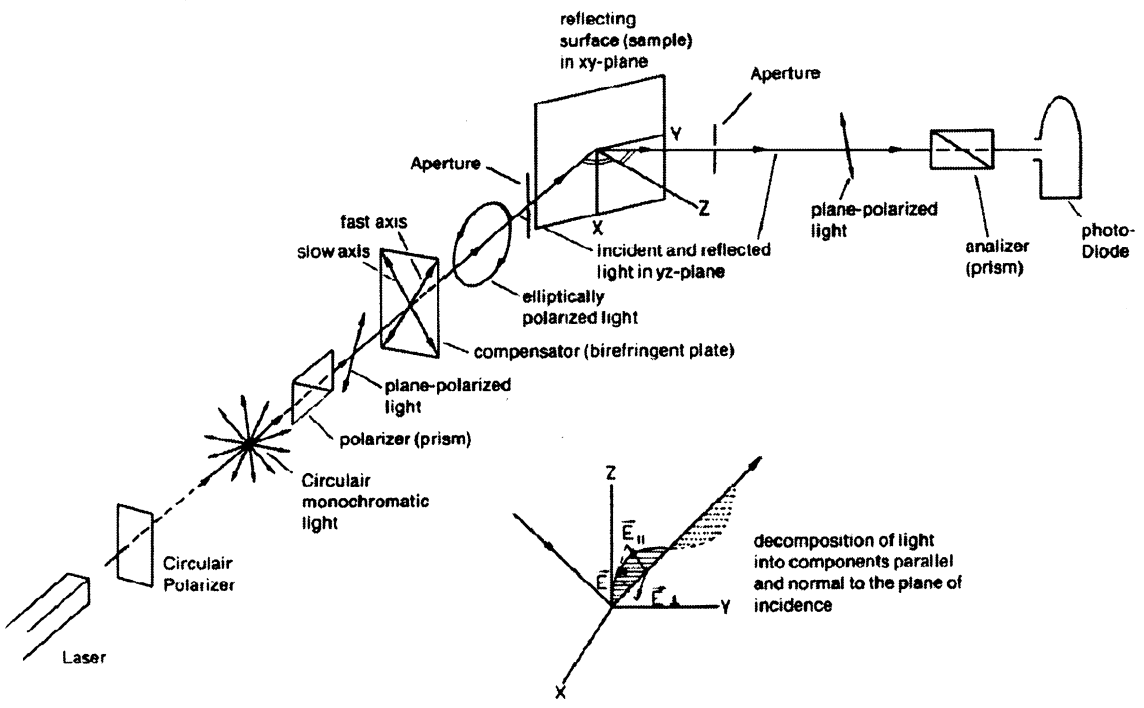

Figure 6. Scheme of the null-ellipsometer setup

The next step of data evaluation involves introduction of a suitable model describing the studied system. For organic layer on solid support we use a simple system consisting of substrate, thin film and medium[30](Figure 7). This system can be fully characterized by 9 variables: angle of incidence, wavelength of the light, thickness of the film and real and imaginary refractive indices of the substrate, thin film and

medium. As one ellipsometry measurement provides two independent values, only two of these parameters can be varied and thus determined during the fitting procedure. The rest parameters must be known in advance. In practice we know the angle of incidence, the wavelength of the light and the complex refractive index of medium. The complex refractive index of the substrate is determined at the beginning of the measurement, when we still have a pure substrate without any adsorbed layer. As the organic compounds are generally non-adsorbing at VIS region, the imaginary part of the refractive index of the layer is zero. The resulting two parameters, real part of the refractive index and thickness of the layer are obtained by fitting.

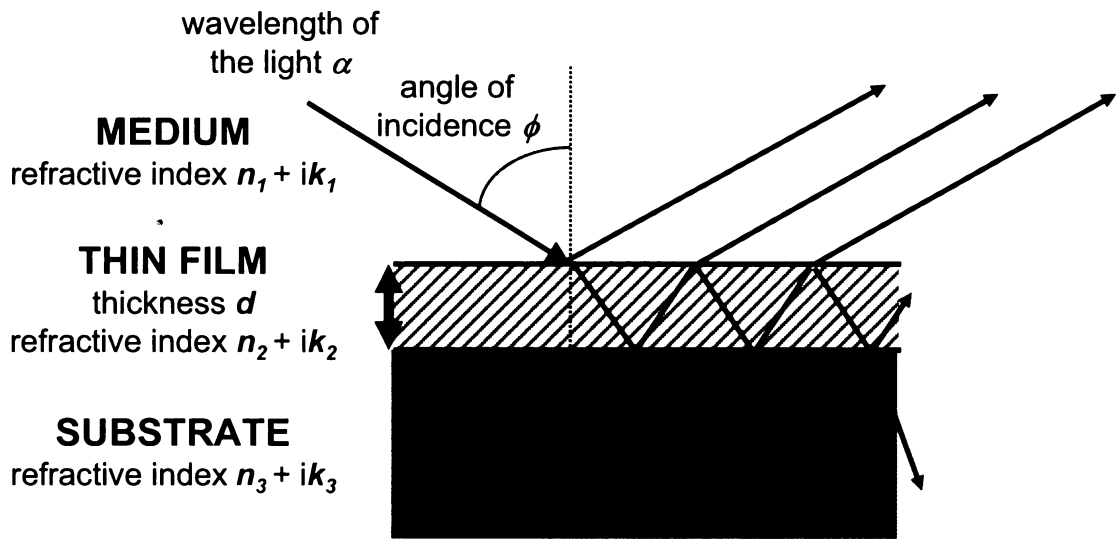

Figure 7. Scheme of the medium-thin film-substrate model used for ellipsometry data evaluation

As was stated above, we obtain the thickness and the real refractive index of the thin organic layer on the support. If we know the chemical composition of the layer, as is the case for lipid or protein layers, the Lorentz-Lorenz relation among the molar refractivities, refractive indices, and the densities of binary mixtures can be used to obtain the mass of the adsorbed layer[28].

A positive feature of ellipsometry is that it can be used for any flat (polished, reflecting) material. The sensitivity of ellipsometry measurements is highly dependant on the contrast among the substrate, film and medium. The contrast means differences in refractive indices. Almost ideal substrate for thin organic films with refractive index n around 1.5 is silicon with its refractive index n around 4. The usage of quartz (n = 1.46), glass (n = 1.5) or mica (n = 1.6) as substrates is possible, but with hugely decreased sensitivity and resolution.

More details about the ellipsometry, the theories and mathematics behind, as well as other experimental realizations and applications can be found in the ellipsometry "Bible" "Ellipsometry and polarized light" written by Azzam and Bashara[31].

1.5 Supported Phospholipid Bilayers (SPBs)

Biological membranes constitute one of the most essential functions and requirements for life. The central role of bio-membranes and membrane functions for living systems is illustrated by the fact that about 60 % of all recently identified human genes are coding for membrane proteins. Cellular membranes are protein-loaded phospholipid bilayers, the characterization of which is still a fundamental question. Phospholipid molecules contain two highly hydrophobic acyl chains and a relatively hydrophilic headgroup. This specific feature causes self-assembly of these molecules into so-called bilayers, consisting of two adjacent sheets of molecules with the headgroups exposed to water, and the chain regions buried into the hydrophobic membrane interior. Many events occur on animal plasma membrane and the importance of understanding them is increasing. Several model systems, mimicking cellular membranes, have been produced, including sonicated, large and giant unilamellar vesicles, black lipid membranes, lipid monolayers at the air-water interface and supported phospholipid bilayers.

Very popular and widely used model systems are supported phospholipid bilayers (SPBs). The interest in SPBs ranges from studies of the dynamic structure of membranes to their self-assembly, lipid-protein interactions, and the construction of membrane-based biosensors.

A multitude of methods has been proposed to create SPBs and related hybrid forms, the most common being Langmuir-Blodgett or Langmuir-Schäfer deposition[32-34], micelle dilution[35, 36] and, in particular, the spreading of vesicles on various preconditioned supports (Figure 8)[37-43]. Each method of preparation has its advantages and drawbacks, the method of choice depends mainly on the targeted lipid and buffer composition and substrate properties.

A very popular technique is the vesicle spreading due to its simplicity and the fact that it often results in defect free bilayers, contrary to Langmuir type preparations. Recently a huge effort was invested into enlightening the mechanism of SPBs creation

by vesicle fusion (Figure 8), many fundamental questions were answered, but still some of them persists[44, 45].

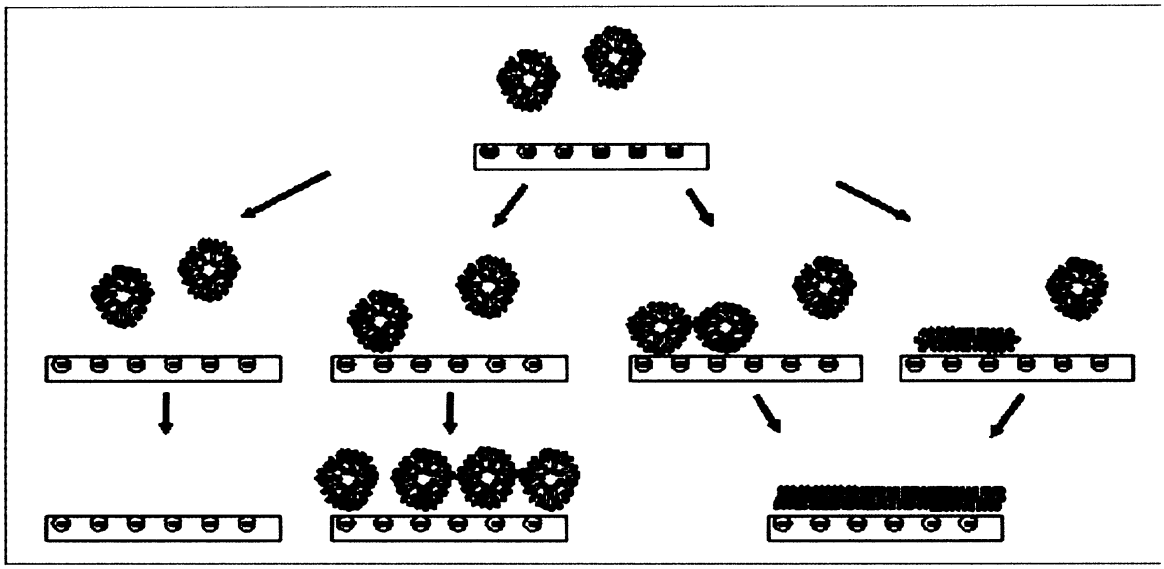

Figure 8. Different pathways of SUVs interaction with hydrophilic support. Adapted from Richter 2005.

The popularity of SPBs stems not only from their easy preparation, manipulation and longterm stability, but also from their accessibility for many sophisticated surface sensitive techniques including ellipsometry[46], total internal reflection fluorescence[4], quartz crystal microbalance with dissipation monitoring[41, 47, 48], impedance spectroscopy[6], atomic force microscopy (AFM)[49-52] and surface plasmon resonance (SPR)[41, 8].

An important feature of SPBs is their two-dimensional fluidity allowing free diffusion in translation and rotation of lipid molecules and lipid-associated proteins. This makes them well suited to analyze lipid domain formation[50, 51, 53, 54], intermembrane interactions[55] or membrane processes such as protein adsorption[29, 56], protein self-assembly[57, 58], protein localization at lipid phase boundaries 87 , and protein function[59].

Chapter 2 Z-scan (Paper I)

2.1 Introduction

Fluorescence correlation spectroscopy has become a very ambitious method. Due to its noninvasiveness (in water solutions under equilibrium conditions), sensitivity and apparent ease of analysis it can be used to help solving many scientific problems, starting from simple concentration and mobility measurements of single fluorescent molecules in vitro to measuring interaction of different fluorescent species directly in living cells.

To fully fulfill these enormous expectations, the method must be very robust, repeatable and free of artifacts. Unfortunately, as recent publications have shown[20, 60, 61], this is not always the case.

The main sources of errors are setup misalignment, sample manipulation, improper data analysis and data over-interpretation.

The objects of our interest are lipid membranes. Our final long-term goal is to be able to perform trustful FCS measurements on membranes of living cells, measurements that would address lipid and membrane-bound protein mobility, protein-membrane interactions and membrane-bound proteins dynamics.

In order to understand the mechanisms occurring in living cells membranes it is essential first to investigate simplified models of biological membranes. Among the mostly used models of biomembranes are liposomes, lipid monolayers at the air-water or oil-water interphase, giant vesicles, supported membranes and others. Every model has its advantages and disadvantages. For FCS studies on membranes there is one main requirement. To follow the diffusion of individual molecules, the membrane must be planar on a scale larger than the size of the laser beam waist, which is in the micrometer range. Moreover, the membrane should be stable and should not move on a timescale of minutes. Systems that meet these requirements most are the supported phospholipid bilayers (SPBs). Other systems one can under certain conditions work with too are giant unilamellar vesicles (GUVs) and lipid monolayers at oil-water interface (ITIES).

2.2 Z-scan

FCS measurements on planar systems show one distinct difference compared to measurements in bulk. Whereas in case of bulk measurements the ACF doesn't depend

on the exact position of the detection volume, in case of planar systems the mutual position of the laser beam and the sample is of a crucial importance. The mutual position determines the shape and the size of the illuminated area and thus also the shape of the resulting ACF.

As the focused laser beam can be described with z-symmetric Gaussian-Lorentzian intensity profile (Equation 3,4,5; Figure 2), the most convenient way is to place the planar sample perpendicular to optical axes to the place of maximum intensity, which means that the sample plane and the focal plane are overlapping.

To place the sample perpendicular to the optical axis is rather easy and moreover the resulting ACF is not very much sensitive to a small tilt. In case of SPBs the proper tilt is aligned using a reflected beam and a xy-objective scan.

Overlapping the sample and the focal plane properly enough is a much more complicated task. The difficulties come from the steep profiling of the focused laser beam. Even a small misalignment causes a huge overestimation of the diffusion time and the particle number. For example 200 nm shift out of focus gives 13% larger values and 500 nm shift gives 81% larger values for both parameters.

The standard way of alignment is to perform an intensity scan in the z-axis and to place the sample (laser beam) to the maximum of the fluorescence intensity[62-64]. As can be shown, this procedure features several drawbacks. The intensity maximum is rather broad, sometimes showing two peaks, often nonsymmetrical and when working on a single molecule level, it's also very scattery. Moreover, to transfer the particle numbers and the diffusion times to absolute concentrations and diffusion coefficients, an additional calibration of the laser beam waist is needed. It's of no surprise, that the results measured by this approach show large standard deviations (> 30 %).

In Paper I we have shown an alternative approach. It's based on the finding that a measurement at only one position cannot reliably recover the correct values. We came with the idea to perform a series of systematic measurements in defined changing z-positions – the so called Z-scan (Figure 9). At every relative z-position of the focus and the sample a standard FCS measurement is performed (Figure 10), the ACF is fitted with the standard 2D model (Equation 10) and the resulting fit parameters are plotted against the relative z-positions.

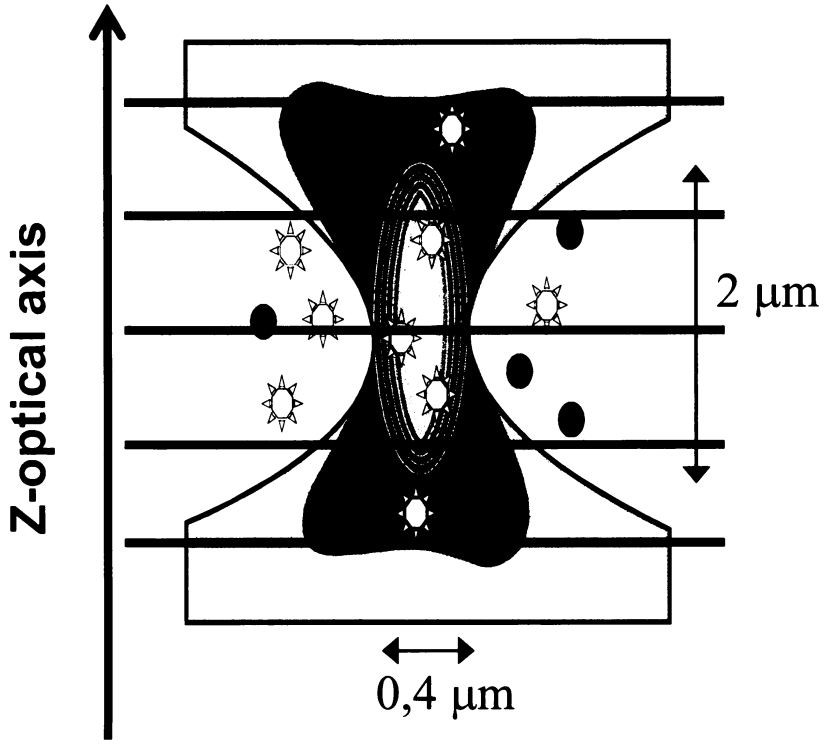

Figure 9. Scheme of the Z-scan. The sample (black line) is systematically placed into parallel and different relative z-positions towards the focal plane.

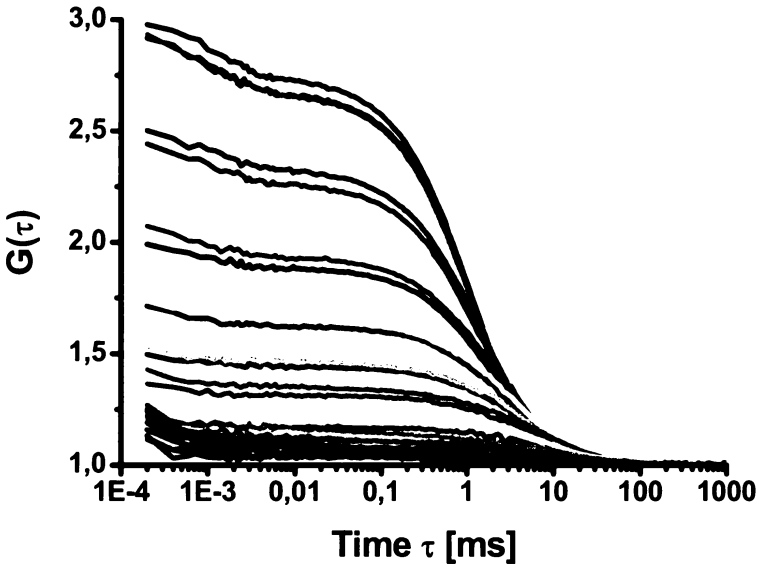

Figure 10. Autocorrelation functions for different sample z-positions measured on SPBs made from DOPC, labeled with Rhodamin Red™ –X DHPE (1:200 000) and created on borosilicate glass

The parabolic dependence of τ_D and N on the z-position extracted from these measurements can be fitted by equations assuming a z-symmetric Gaussian-Lorentzian beam profile (Equation 11, 12) (Figure 11). The fit gives three parameters: the real position of the overlap of the sample and the focal plane z_0, the laser beam waist w_0 and directly the diffusion coefficient D or concentration c.

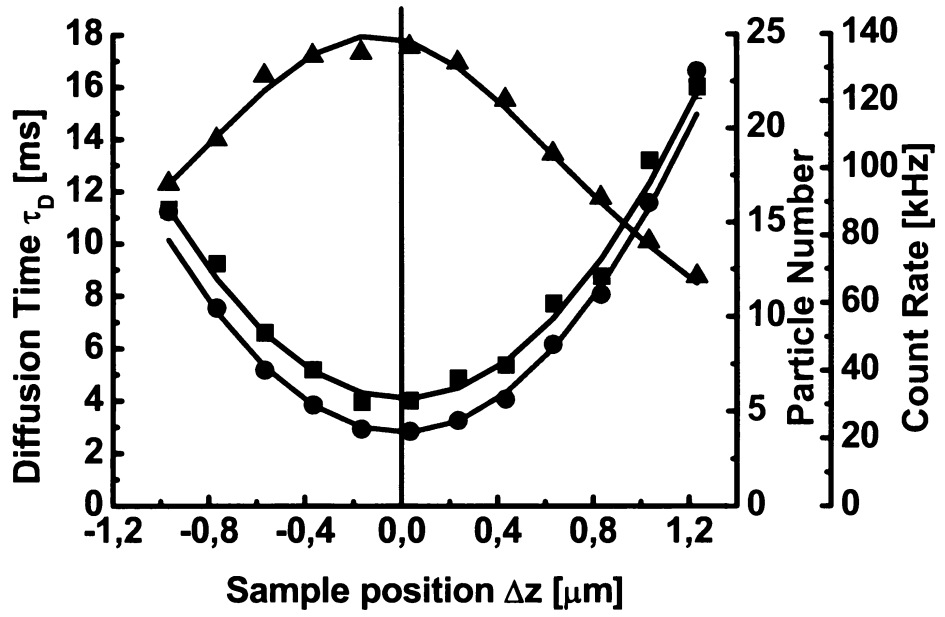

Figure 11. The dependences of diffusion time τ_D, particle number N and count rate (fluorescence intensity) F on the sample position Δz for SPBs (made from DOPC, labeled with Rhodamin RedTM –X DHPE (1:200 000) and created on borosilicate glass)

The major advantages of the presented Z-scan are:

1. Precise localization of the sample
2. Withdrawal of external calibration of the focal volume size
3. Improved precision of diffusion coefficient determination down to relative standard deviation of 5%
4. Distinguishing between lateral diffusion and other processes

An interesting question is the role of the pinhole. For bulk measurements the pinhole is assumed to cut off the out-of focus fluorescence and by this create 3D-Gaussian detection volume. But for 3D-Gaussian detection volume the parameters particle number N and diffusion time τ_D should not depend on the z-position of the sample. Our measurement thus shows that this approximation cannot be used for 2D samples. We studied the effect of the size of the pinhole on the resulting parameters (Figure 12). The larger the pinhole is the higher the overall countrate CR (intensity) and particle number N are. The diffusion time τ_D and counts per molecule CpM reach their plateau for the pinhole diameter 45 μm in image plane, which is 1.125 μm in focal plane and is approximately 2 times more than the diameter of the laser beam. The continuous increase of the particle number N can be explained by the increasing background, which effectively increases the apparent particle number N[65]. The important fact is that diffusion time τ_D and counts per molecule CpM reach constant values. The optimal

pinhole size is thus 45 μm, where stable values for diffusion time τ_D are reached and the background is the smallest.

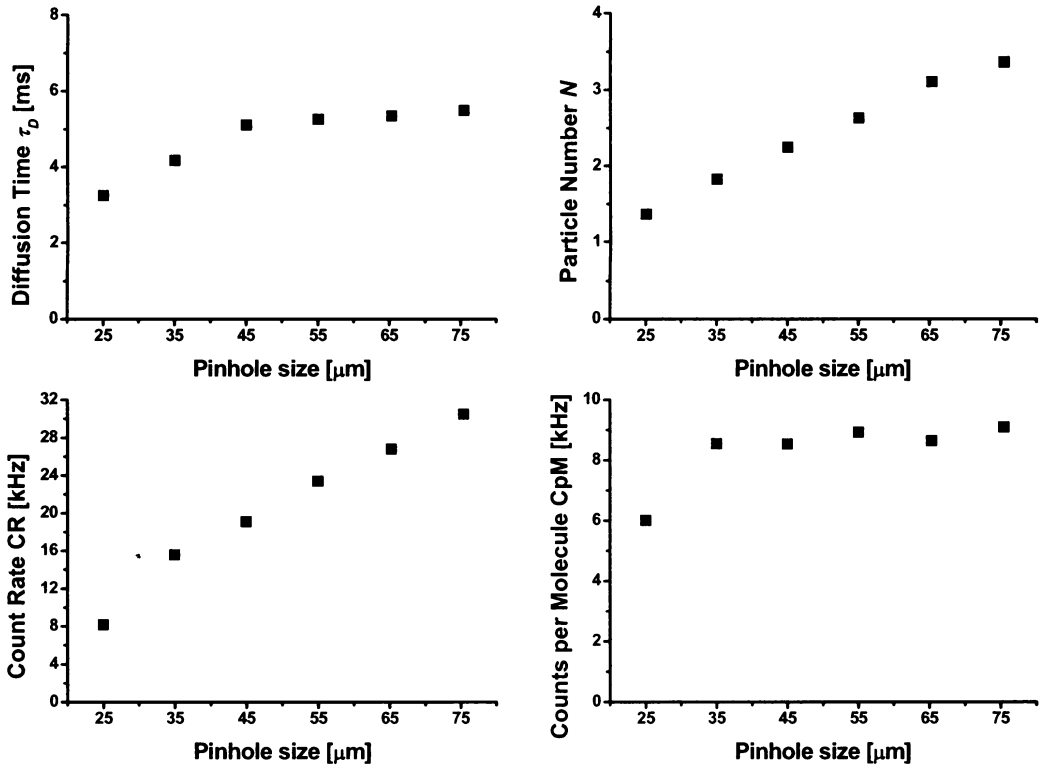

Figure 12. Influence of the pinhole size on Z-scan measurements

2.3 Comparison of one- and two- photon excitation

In order to prove our findings and interpretations, a Z-scan experiment was also performed with a two-photon excitation setup (Prof. Yves Mely, Strasbourg, France). The sample was identical as in Paper I, SPBs (DOPC/DOPS 4/1 labeled with Rhodamine Red-X DHPE 1:200 000) in HEPES buffer on mica, the only difference was the mode of excitation. Again parabolic behavior was found, but this time the parabola is more open due to the wavelength of the excitation (870 nm compared with 543 nm).

Very surprising was the comparison of diffusion coefficients D given by both instruments. The diffusion coefficient D from the two-photon excitation was 3 times larger than the diffusion coefficient D from one-photon excitation under standard instrumental setup. Later experiments studying the influence of the used laser intensity

on the resulting fit parameters revealed a huge dependence of apparent diffusion time τ_D on the used intensity (Figure 13).

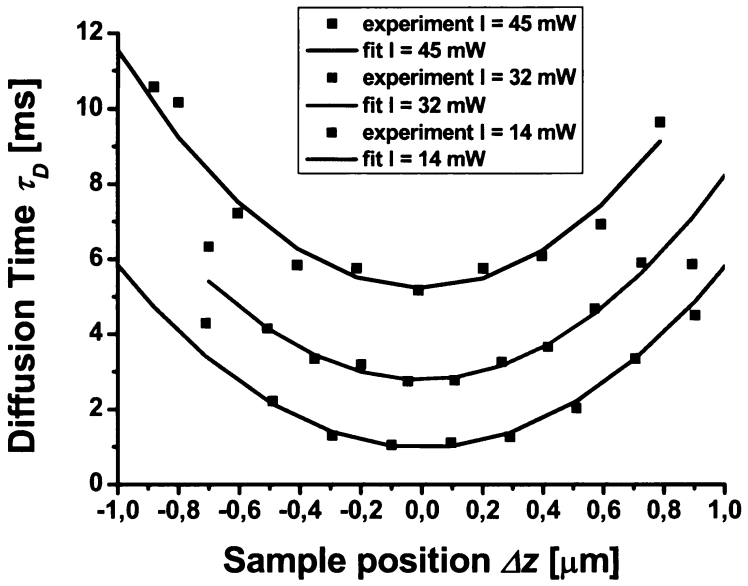

Figure 13. Two-photon Z-scans of Rhodamine Red-X DHPE in DOPC/DOPS 4/1 SPBs on mica for three different excitation intensities (I = 45 mW, 32 mW and 14 mW).

There are two effects connected with the used laser power which influent the FCS parameters. The first one is an optical saturation and the second one is a photobleaching. Optical saturation occurs when the excitation power increases to values so that molecules within the detection region are to a significant extent not in the ground state but in the excited state or the triplet state. As was pointed out by Enderlein[21, 66], the saturation causes non-linear response of the fluorescence intensity on the excitation intensity, widening the effective detection volume and thus increasing the apparent N and τ_D. The saturation is an equilibrium process and can thus be mathematically described and treated within FCS theory. Photobleaching means an irreversible photodestruction of the fluorescent molecule. It causes an apparent shortening of the diffusion time, as the molecule gets destroyed before it diffuses through the detection volume. There are some articles[67-72] trying to incorporate the photobleaching into FCS theory and by this use FCS to study the photobleaching rates and experimental conditions influencing it. A precise incorporation of photobleaching into FCS theory is unfortunately impossible due to the irreversible non-equilibrium nature of the bleaching process.

However some conclusion concerning the photobleaching can be made. The rate of the photobleaching process determines how many excitation-emission cycles on average the dye molecule survives and for how long the molecule can be observed under the used excitation power. For FCS this means that the average photobleaching lifetime should be longer than the diffusion time. As soon as it is opposite, the apparent diffusion time gets shorter, becomes the photobleaching time and we lose information about the diffusion. The photobleaching phenomenon is thus a limiting step for slow diffusion measurements.

In Figure 14 you can see the intensity dependences for one- and two- photon excitation. For low excitation intensities the diffusion time τ_D is becoming stable and gives us approximately the same diffusion coefficients D for both excitation modes. A remarkable difference between the two modes of excitation is the extreme intensity sensitivity and orders of magnitude lower counts per molecule CpM at stable regions for the two-photon case.

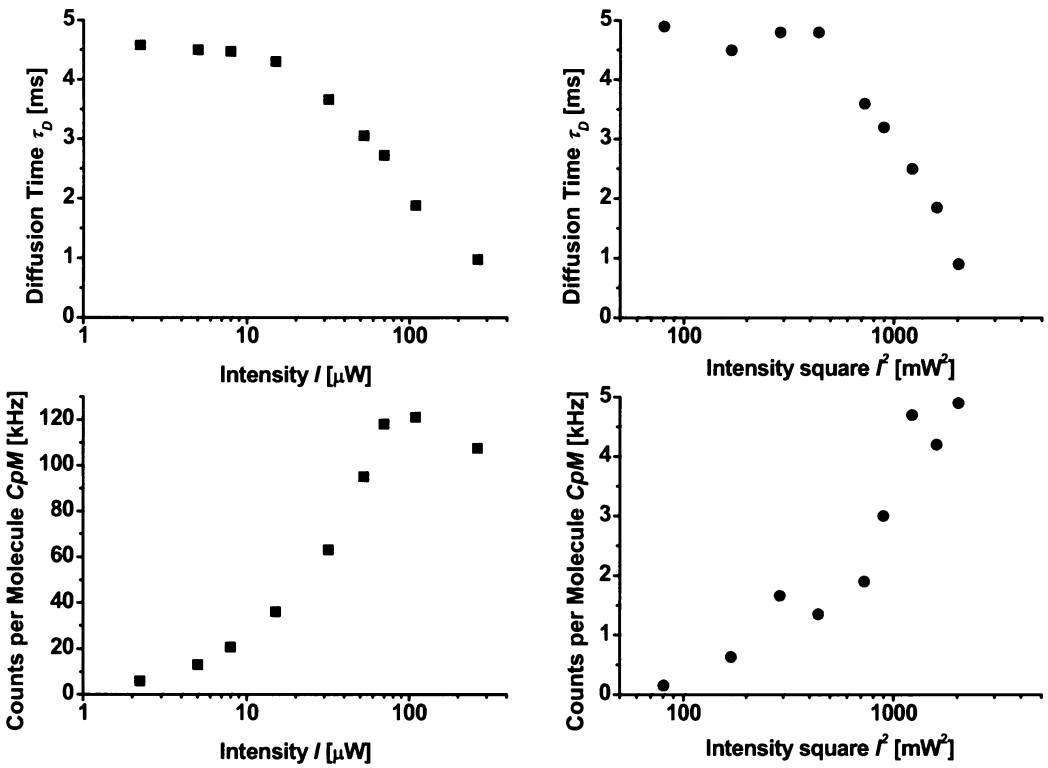

Figure 14. Influence of the used excitation intensity on the FCS parameters diffusion time τ_D and counts per molecule CpM for one and two photon excitation. Data are shown for Rhodamine Red-X DHPE in DOPC/DOPS 4/1 SPBs on mica.

These observations can be explained by different mechanisms of photobleaching. In one photon case it's generally assumed and partially proved that the photobleaching happens from the triplet state and is linearly dependant on the used excitation intensity, whereas in the two-photon case higher order processes (radical creation, absorption of additional photon) are involved resulting in more than quadratic dependence of photobleaching rate on the used excitation intensity[67]. In case of Rhodamine Red-X DHPE new fluorescent species are created under high excitation power, which is indicated in the emission spectra collected directly from the excitation volume (Figure 15).

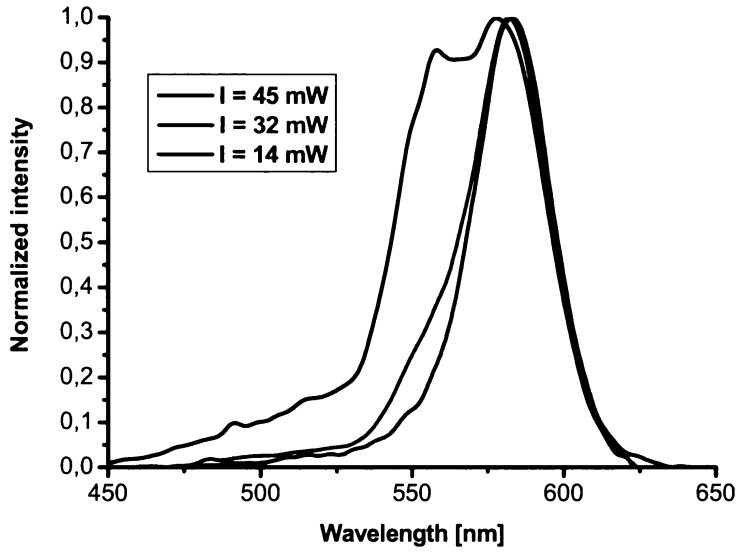

Figure 15. Two-photon fluorescence emission spectra of Rhodamine Red-X DHPE in DOPC/DOPS 4/1 SPBs on mica under three different excitation intensities (I = 45 mW, 32 mW and 14 mW).

Our goal was neither to discover the photobleaching mechanisms nor to develop a theory describing the effect of photobleaching on ACF curves. Our goal was to find the optimal experimental conditions where both the saturation and photobleaching are negligible and still we have high S/N ratio, and to show a way how to find these conditions.

The presented results show that although the two-photon excitation has several advantages like deeper penetration in tissues and lower overall sample photobleaching, for measuring slow motions it's less advantageous than the one photon excitation due to much higher photobleaching rates.

2.4 Multi-focus FCS (Paper VIII, Paper IX)

As mentioned in the previous chapters, the diffusion coefficients measured by FCS are prone to many experimental artifacts coming mainly from the uncertainties in the detection volume (illuminated area) size. The measured diffusion time cannot thus be precisely transferred to the diffusion coefficient. To overcome this problem, the so-called multi-focus FCS was suggested by Enderlein and experimentally realized by Dertinger. For testing of this newly designed setup measurement of lipid diffusion in SPBs was performed and compared with Z-scan approach[Paper VIII, Paper IX].

There are two key ideas behind the multi-focus FCS. The first idea is to replace the uncertain size of the detection volume used in the standard FCS by another precisely measurable parameter – to introduce two or more partially overlapping laser foci, mutual distances of which are measurable by CCD camera and serve as an exact ruler. Assuming Gaussian intensity profiles of the focused laser beams in the xy-plane (which is a very reasonable assumption confirmed by the reflected beam image analysis), the ratio of cross- and auto-correlation functions of the two overlapping foci contains a term, which is dependant on the distances of the foci:

$$\frac{G(\tau,\delta)}{G(\tau,0)} = \exp\left(\frac{-\delta^2}{4D\tau+\omega^2}\right) = \exp\left(\frac{-\delta^2/4D}{\omega^2/4D+\tau}\right) \qquad (24)$$

where δ is the distance between the foci, ω is radius of the foci, D is diffusion coefficient, $G(\tau,0)$ is autocorrelation function and $G(\tau, \delta)$ is cross-correlation function between two foci.

Knowing the ratio of cross- and auto-correlation functions for two or more foci distances, the radius of the foci can be eliminated from the fitting procedure and diffusion coefficient directly determined.

The second key idea is connected with the practical realization. The main question several groups were fighting with is how to separate the fluorescence signal from the overlapping foci. A recent technical development in the pulsed diode laser and detection technology enabled a very elegant solution. Instead of using continuous-wave lasers, two or more sequentially pulsed diode lasers with overall repetition frequency up to 80 MHz and pulse width less than 100 ps are used. The fluorescence photons are detected by two detectors (afterpulsing removal) and the detection events are stored in TTTR mode (Figure 16). Photons coming from different foci are separated on a nanosecond time scale, which enables to separate them in the subsequent analysis

(Figure 17). This quasi-simultaneous setup thus gives us the desired independent intensity traces for each focus.

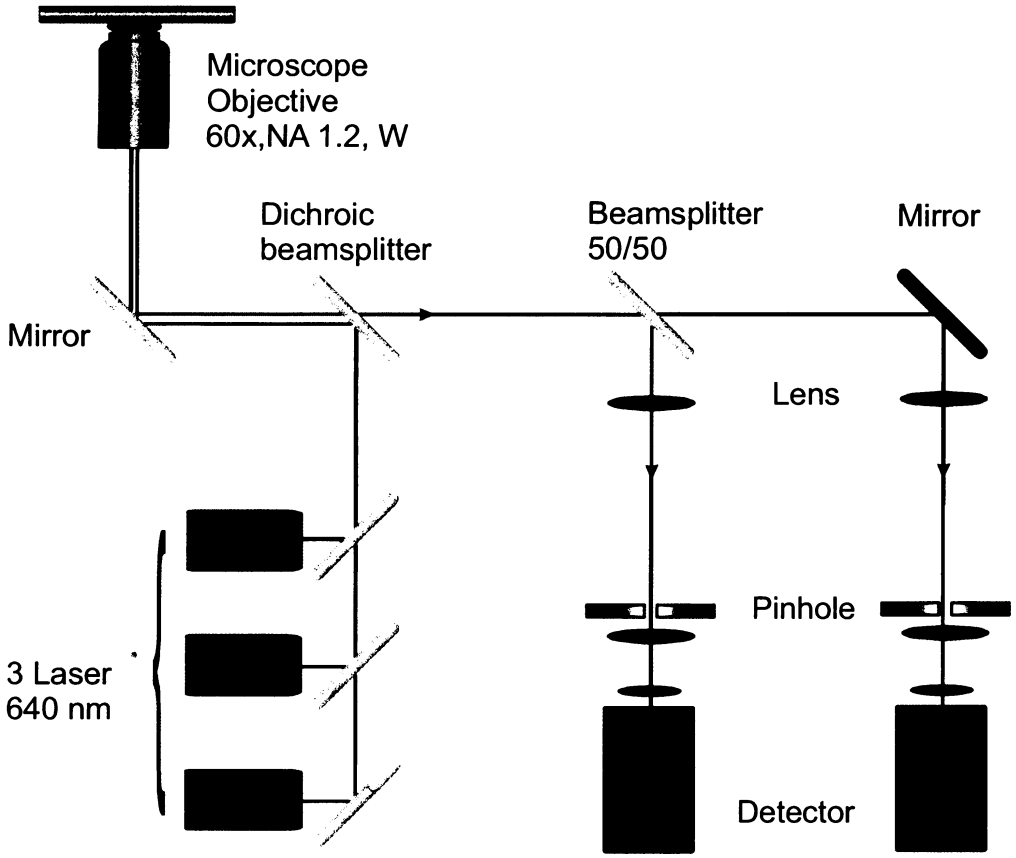

Figure 16. Scheme of the multi-focus setup

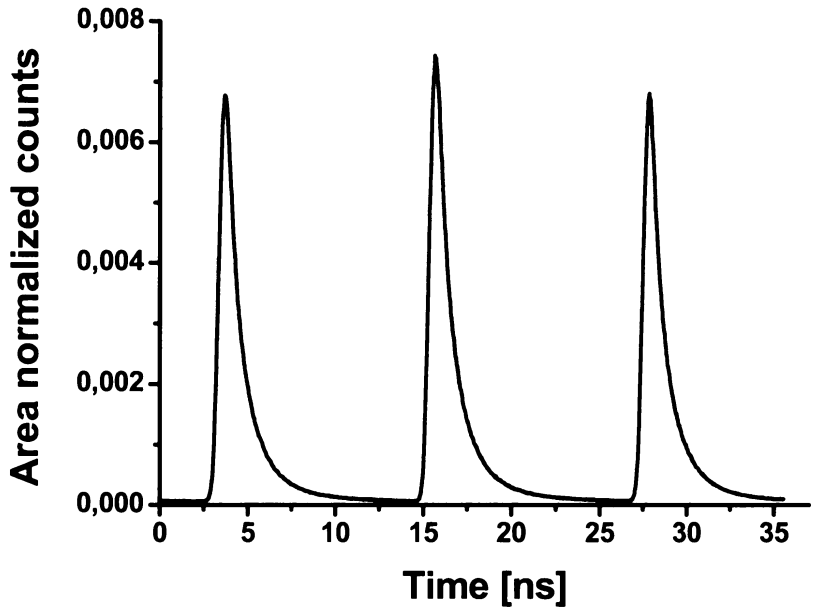

Figure 17. Area normalized histogram of relative photon arrival times - DiD in SPBs measured by the multi-focus setup

The test measurements were performed on DOPC/DOPS 4/1 SPBs on mica labeled with a short lifetime lipid analogue DiD. Three red diode lasers (LDH-P-635, PicoQuant GmbH, Berlin, Germany) were sequentially pulsed with overall repetition frequency 80 MHz, which means that a single diode pulsed with a frequency 26,7 MHz and pulses between two different diodes were separated by 12,5 ns, which is an interval large enough for DiD dye with its lifetime 1 ns (Figure 17). The laser foci were aligned to have the same sizes, to create an irregular triangle in xy-plane in order to have three foci distances for subsequent analysis, and to have the same z-positions (Figure 18). The sample was then measured in a z-scan manner, which means that a series of measurements in different z-positions of the sample was performed. Each measurement thus contains the complete data for multi-focus analysis and each focus can be z-scan analyzed for the whole series.

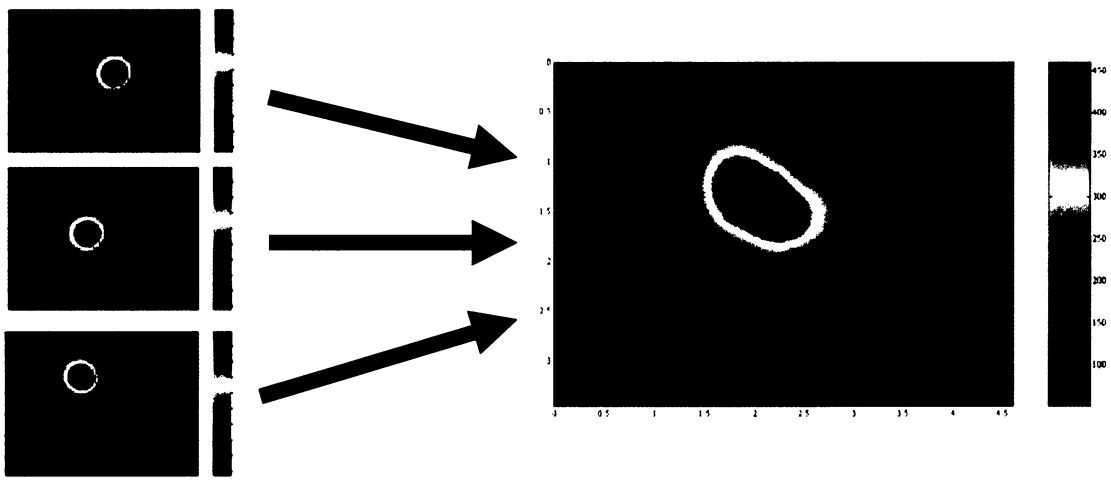

Figure 18. Back-reflected images of single foci and of their overlap. The black dots in the overlap image are centers of each focus determined by fitting the intensity profiles in the single images.

A comparison of Z-scan and multi-focus FCS revealed that diffusion coefficients obtained by these two approaches were slightly different. The Z-scan gave 1.9 ± 0.3 $\mu m^2 s^{-1}$, multi-focus FCS 2.9 ± 0.3 $\mu m^2 s^{-1}$, but the experimental data were very difficult to fit. Further study revealed that the problems may have been caused by improper optical alignment and mainly by photophysics of the used DiD dye, by its cis-trans photo-isomerization and photobleaching.

In order to overcome the mentioned problems, new setup was constructed, and a new labeled lipid (DOPE labeled with Atto655-NHS-ester) was used[Paper IX]. This time only two linearly polarized pulsed lasers (LDH-P-635, PicoQuant GmbH, Berlin, Germany) are combined by a polarizing beam splitter to yield a single beam with

crossed polarizations. This light is sent through a single-mode optical fiber for mode cleaning (improving quality of the focused beam). After exiting the fiber, the light is re-collimated, reflected by a dichroic mirror and passed through a differential interference contrast (DIC) prism. The prism deflects the light from the two lasers into slightly different directions, so that after focusing through the objective one obtains two laterally shifted but overlapping laser beams with parallel propagation axes. The distance between the beams is uniquely defined by the chosen DIC prism and is in our system equal to 400 nm, as measured by scanning the point spread functions with fluorescent beads. Fluorescence excited within the foci of these beams is collected by the same objective, passed through the DIC prism and the dichroic mirror, and focused into a single circular aperture which is positioned symmetrically with respect to both focus positions and chosen large enough to let easily pass the light from both foci. After the pinhole, the light is re-collimated, split by a non polarization sensitive beam splitter cube, and focused onto two single-photon avalanche diodes. The rest is the same; the signal from detectors is processed in TTTR mode by TimeHarp200 board and analyzed as described above.

The improved setup and the new fluorophore lead to the overall improvement of measurement characteristics, giving identical diffusion coefficients 3.3 ± 0.2 $\mu m^2 s^{-1}$ at 22 °C for both methods. This time the setup was tested on DOPC SPBs on glass.

The multi-focus FCS was shown to be a valuable alternative to standard one-focus FCS. The advantage is its insensitivity to precise z-positioning, as it depends only on the mutual distance of the laser beams and no Z-scan is thus needed. On the other hand, to obtain good measurement statistics longer measurement times are required, and due to longer cross-correlation times, the times the fluorophore stays illuminated, it's more susceptible to photobleaching artifacts.

2.5 Z-scan on living cells – a way to study confined diffusion (Paper V, Paper X)

After the successful application of Z-scan on model lipid membranes, the next step was to introduce it also to the living cell research. Because Confocor 1 has no scanning unit and thus does not enable cell measurements, the first cell measurements were done in collaboration with Prof. Yves Engelborghs from University of Leuven, Belgium. The measurements were done on living oligodendrocytes, which are the myelin-producing cells of the central nervous system, using Confocor 2 apparatus.

The original aim was just to improve the cell-membrane FCS measurement quality, which means precise localizing of the membrane, avoiding the external calibration and resolving between membrane and free space diffusion, and by these improvements to enable systematic studies on cells (cell-membrane response to different stimuli)[Paper X]. But apart from this, another very useful feature of Z-scan was discovered.

The plasma membrane of living cells is heterogeneous in structure and may contain microdomains, which can impose constraints on the lateral diffusion of its constituents. The size of these microdomains is under diffraction resolution limit of visible light optical methods. Prieto et al[73-75] use indirect method of Fluorescence Resonance Energy Transfer (FRET) to study the size of the microdomains and their phase behavior on model systems. FCS is used to directly investigate the labeled lipid diffusion in different phases of lipid membranes. When the domains are larger than the optical resolution, interpretation of the results is rather straightforward[76]. In the case of microdomains, where the signal comes from both phases and the resulting ACF is governed by diffusion in fluid phase, in gel phase and by interchange between these phases, standard FCS measurement gives ACF that can be very well fitted with the standard one component 2D diffusion model. Thus it is impossible to decide whether we have a system with slow diffusion and without microdomains or a system with fast diffusion and with microdomains. Very recently L. Wawrezieck et al[77] described a method to probe the nature of the lateral microheterogeneities of the membrane by varying the beam size in the FCS instrument. The dependence of the width of the autocorrelation function at half maximum, i.e. the diffusion time, on the transverse area of the confocal volume gives information on the nature of the imposed confinement.

We show that the Z-scan is an alternative approach which yields essentially the same information and which can readily be applied on commercial FCS instruments[Paper V]. The change of the illuminated area size is not performed by changing the underfilling of the objective, but by simple movement of the focus in z-axis. The measured diffusion time is plotted against the measured particle number, which serves as an indicator of the illuminated area size. The intercept of the linear fit of this dependence with the y-axes (diffusion time axes) tells us about the nature of the confinement. For model system of SPBs it's close to zero, whereas for the cells it's significantly different from zero and positive, suggesting hindered diffusion by rafts.

2.6 Comparison of lipid diffusion in supported and free standing membrane (Paper VI)

A long lasting question in SPBs research is how much is the diffusion of the lipids in SPBs influenced by the presence of the support. It is known that the diffusion of transmembrane proteins is often highly restricted by the support[78]. The mobility of lipids themselves in SPBs was expected to be slowed down as well due to the frictional forces between the lipids and the support[79]. Surprisingly, there was no direct experimental conformation of this theoretical expectation. There are multiple reports on the values of diffusion coefficients in supported membranes[80, 81] and in free standing membranes – giant unilamellar vesicles (GUVs)[63, 76], but none of them compared these two systems directly, under identical conditions. A comparison of the reported values is thus hampered by differences in experimental conditions (lipid composition, buffer, temperature).

The main problems of such a comparison are conditions used for creation of SPBs and GUVs. Whereas GUVs require low ionic strengths, glucose-sucrose solutions for sedimentation and stabilization[82] and low temperatures suppressing bending and undulations, SPBs are mainly prepared at high salt concentrations, without glucose or sucrose and at room temperatures.

In Paper VI we performed an absolute comparison of diffusion coefficients in supported and free standing bilayers using the Z-scan. The experiments were carried out using the new confocal scanning microscope MicroTime 200 (PicoQuant, Germany). The absolute comparison means that all experimental conditions were identical – both membranes were prepared from the same lipid mixture and the measurements were performed in one cuvette, having the buffer composition, temperature and instrument setup identical.

The result is shown in Figure 19. The diffusion coefficient of β-C8-BODIPY® 500/510 C5-HPC in DOPC bilayers is 7.8 ± 0.8 $\mu m^2 s^{-1}$ for free standing form (GUVs) and 2.9 ± 0.3 $\mu m^2 s^{-1}$ for supported form (SPBs) at temperature 16°C.

The observed large difference of lipid mobility in free and supported membranes may by explained by weaker, but still substantial, frictional coupling between the support and the inner leaflet than between the bilayer leaflets[83, 84]. The precise nature of the coupling remains unclear, as can be documented by the fact that a fluid lipid

monolayer retains its mobility even when deposited on immobile gel phase lipid layers[Paper III].

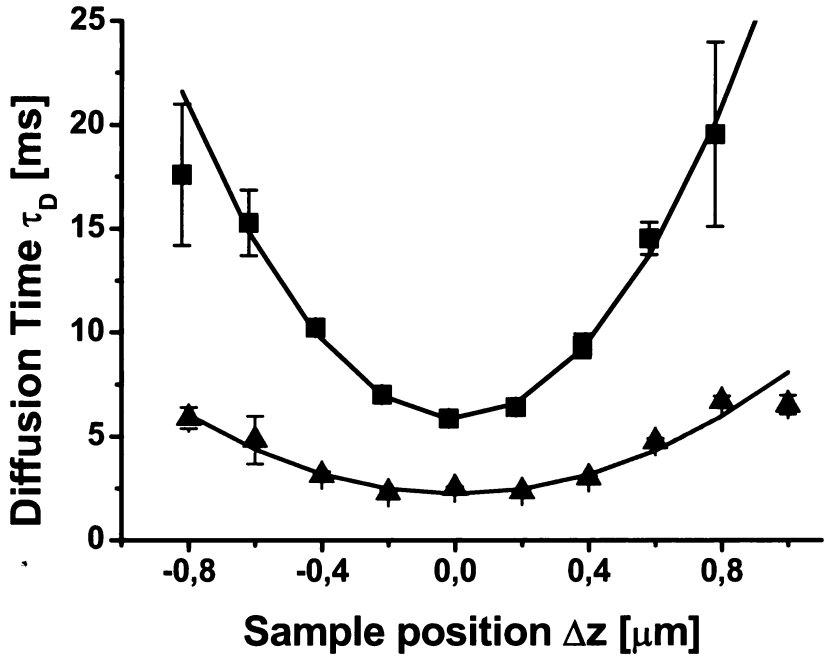

Figure 19. The typical dependence of the diffusion time τ_D on the z-position of the sample relative to the laser beam for GUVs (red triangles) and SPBs (black squares).

Another possible mechanism for slowing down the lipid diffusion might be the partial restriction of the motion of the lipid molecules in the plane of the bilayer caused by the (electrostatic) interaction with a flat support. As a consequence, lipid molecules partially lose one degree of freedom how to pass by the adjacent molecules which results in a slower diffusion.

2.7 Combining FCS with ellipsometry (Paper IV, Paper VII)

As was shown in the previous chapters, FCS is a powerful tool to study SPBs properties by measuring lipid diffusion. The problem is that it always requires fluorescent labeling, it works under equilibrium conditions and the experiment takes a rather long time. Moreover, the usual experimental setup constrains efficient control of experimental conditions (temperature, stirring, flow conditions, etc.). SPBs are model systems that due to the presence of the support can be studied by many surface sensitive techniques, for example by AFM, ellipsometry, SPR, QCM-D and some more. To

enhance our possibilities in SPBs research, we decided to combine FCS with at least one of the surface sensitive techniques. The most versatile method concerning the used supports is ellipsometry. Any support with a refractive index different from the refractive index of water and lipid bilayer can be used. The ellipsometry provides information about the thickness and the refractive index of thin layers adsorbed onto the supporting surface. The big advantages of the ellipsometry are its non-invasiveness, no need of labeling and its ability to monitor the kinetics of adsorption, desorption or phase change with less than second time resolution.

Our first FCS experiments on SPBs suffered from the fact that we were not absolutely sure that the SPBs are completely created and defects free. From literature it is known that SPBs creation by SUVs fusion depends on many experimental factors including the used surface, charge of the lipid mixture, buffer, temperature, SUVs concentration and stirring conditions. In cooperation with Prof. Wim Hermens from Maastricht, Netherlands, we studied by ellipsometry the mechanisms of SPBs creation from neutral and negatively charged SUVs on mica, glass and silicon in HEPES buffer with or without calcium. An extreme influence of calcium on SPBs creation on mica was observed. Without calcium no SPBs were created, instead of that weakly bound vesicular layer was created. The so-called critical coverage phenomenon was identified for SPBs creation on silicon. A positive finding was that for any of these surfaces a fast diffusion limited kinetics leading to complete surface coverage was observed under standard conditions (10 mM HEPES, 150 mM NaCl, 2mM CaCl2, pH 7.4)[Paper IV].

Having a good experience with the ellipsometry technique, we bought a single wavelength null-ellipsometer to our lab in Prague. Apart from the ellipsometry research itself we wanted to combine the ellipsometry with FCS as much as the different requirements of these techniques allow. There are two motivations for this combination. The first is the study of dynamics properties of membranes with different lipid compositions. As the SPBs creation depends on the lipid composition, we need to prove for every lipid mixture that the SPBs are created. The best approach is creating the SPBs on ellipsometer and then using the same membrane for FCS experiments. The second motivation is the characterization of protein-membrane interactions. The combination of these methods enables to directly relate the absorbed protein mass with changes in lipid or protein diffusion coefficients. The scheme of the constructed cuvette for combined FCS-ellipsometry experiments is in the Figure 20. This cuvette does not enable real simultaneous FCS and ellipsometry measurements, but enables to measure the same

sample in the same cuvette by both methods without a need of sample transfer, with a short time for cuvette relocation.

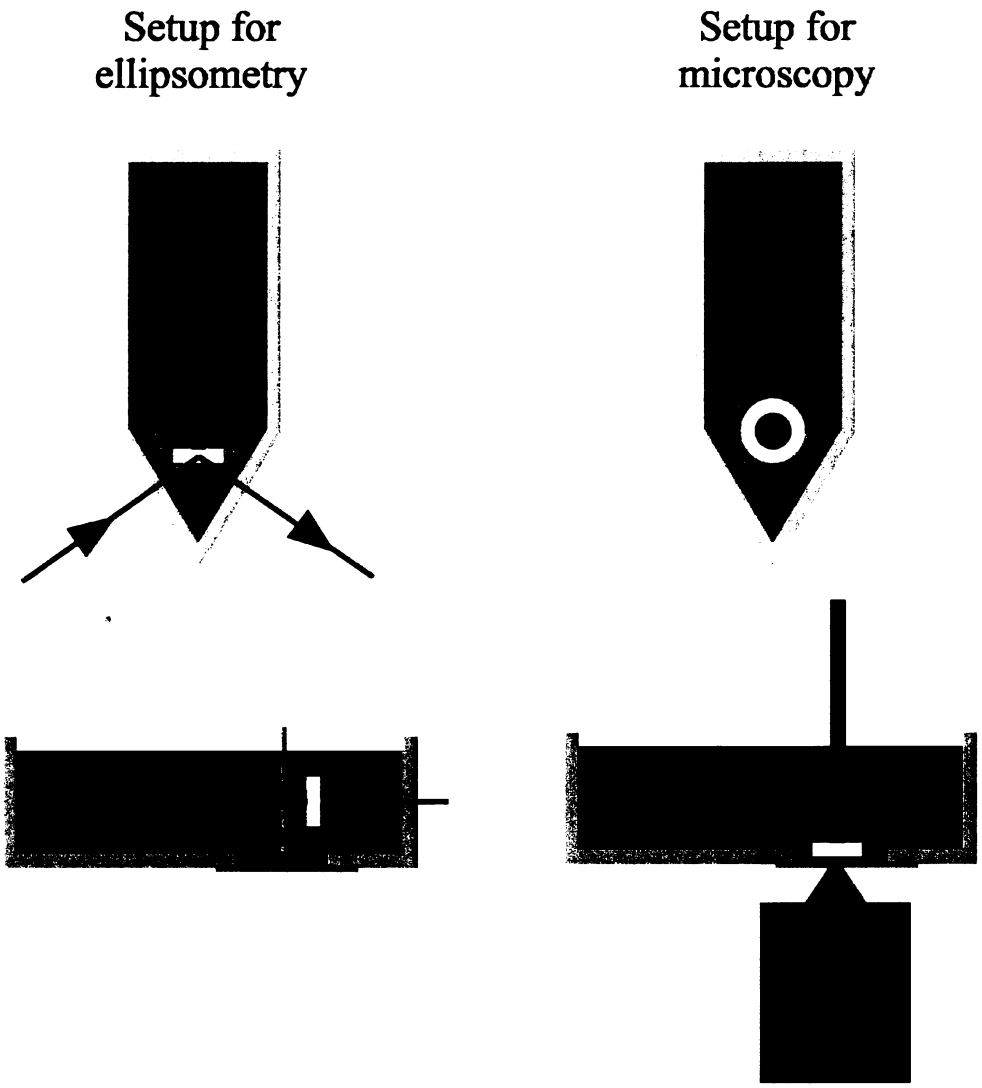

Figure 20. Cuvette for combined ellipsometry and FCS measurements. The sample is in vertical position for ellipsometry measurements (the sample holder is horizontal) and in horizontal position for FCS measurements (the sample holder is vertical). The advantage is that the sample does not need to be transferred, just turned, thus decreasing the risk of the sample damage.

A topic the combined FCS-ellipsometry experiments are extremely useful for is the study of the interaction of antimicrobial peptides with SPBs. First FCS results about the influence of the protein binding on the mobility of the SPBs are presented in Paper VII. We continued in that study and a new manuscript containing very detailed results comparing the different mechanisms of interaction with membrane for antimicrobial peptides Melittin, Magainin 2 and Cryptdin-4 is being prepared.

Chapter 3 Implementation of Time-Resolved Fluorescence Correlation Spectroscopy (Paper II)

3.1 Introduction

It has been shown in the previous chapter, that the standard one-color confocal FCS is a powerful tool to follow diffusion of single fluorescent species. But what if we are interested in following the diffusion of more than one species, or we want to study conformational changes and chemical reactions? What are the requirements and limitations?

To resolve two different diffusing fluorescent species by ACF fitting, their diffusion coefficients must differ at least by factor of 1.6[25] under favorable conditions, which means for globular molecules a factor 4 difference in their molecular weight. In real experiments, where the shape of ACF is influenced by additional non-diffusion processes, this means that the standard one-color confocal FCS is almost unable to follow simultaneously two different species with similar size, to study protein-protein interactions or small conformational changes.

The source of information about the studied system in the standard one-color confocal FCS is just the fluorescence intensity trace. To overcome the above mentioned limitations, other characteristics the detected photon can be described with must be used. These include excitation and emission wavelength, polarization and excited state lifetime.

The first developed method using the additional information is the dual-color fluorescence cross-correlation spectroscopy[13]. It uses two or more fluorophores with different spectral properties and separates the signal coming from their mixture by using two excitation wavelengths and at least two spectrally different detection channels. The main limitations of this method are the precise position and size alignment of the overlapping foci and the spectral crosstalk between the dyes. The architecture of our Confocor 1 instrument doesn't allow the required hardware upgrade.

Another advanced method for multicomponent FCS analysis, the so called Time-Resolved Fluorescence Correlation Spectroscopy (TR-FCS)[14], arose from the combination of Time-Correlated Single Photon Counting (TCSPC) and Fluorescence Correlation Spectroscopy (FCS). The main idea is to use different excited state fluorescence decays to separate ACF contributions from a mixture. As it uses the

excited state lifetime information, it's alternatively called Fluorescence Lifetime Correlation Spectroscopy (FLCS).

The species to be separated are required to have similar spectral properties (the fluorophores must be excitable by the same laser and the emitted light must be detected by the same detector), but must differ in their excited state decay. The technical requirements are picosecond pulsed lasers and picosecond time-resolved detection in the so-called time-tagged time resolved (TTTR) data acquisition mode.

3.2 Hardware upgrade

The hardware changes required for the picosecond excitation and time-resolved detection are depicted in the Figure 21 and are fully compatible with Confocor 1 architecture. The standard continues-wave lasers must be replaced by pulsed ones, a fast single photon detector and a TTTR data acquisition unit instead of an online hardware correlator must be introduced as well. To upgrade our confocal microscope Confocor 1, we used picosecond pulsed diode lasers LDH-P-C-470 and LDH-P-635 with single PDL 800-B laser driver (PicoQuant GmbH, Berlin, Germany), optimized sets of optical filters[83] (Chroma Technology, Rockingham, USA) consisting of an excitation filter (HQ457/18, z640/20x), a dichroic mirror (z470rdc, z640rdc) and an emission filter (HQ515/50, HQ685/50), fast single photon avalanche diode SPCM-AQR-13-FC (Perkin-Elmer, Fremont, USA) and TCSPC board TimeHarp 200 (PicoQuant GmbH, Berlin, Germany).

The presented hardware setup together with the software provided by PicoQuant (MicroTime 200, TimeHarp 200 basic software) already enabled advanced applications like simultaneous TCSPC and FCS measurement (see chapter 3.4). After the development of our own fast correlation algorithm enabling photon weighting the Time-Resolved FCS experiments become possible.

3.3 Fast correlation algorithm enabling TR-FCS data treatment

Although the definition of the correlation function is rather easy (Equation 1), to calculate its values from experimental data is not a trivial task at all. The standard number of detected photons is 100 000 per second, which is for 10 minutes lasting measurement 60 millions photons. The processes under investigation happen on

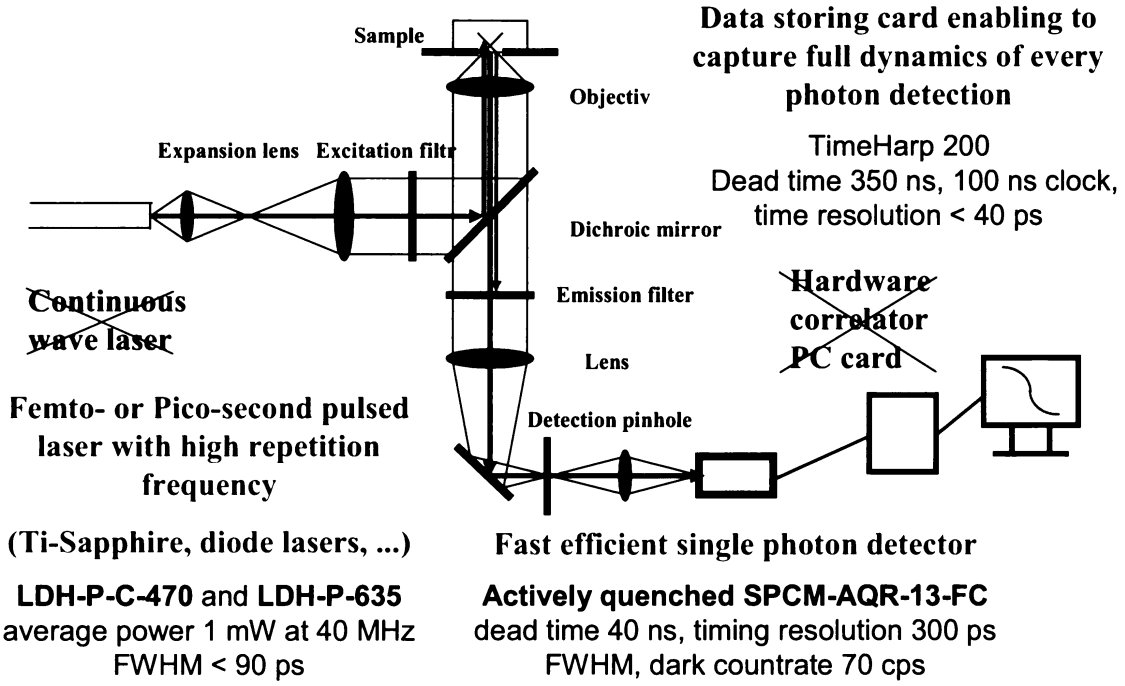

Figure 21. Scheme of the hardware upgrade necessary for TR-FCS measurements

microsecond to second time scale. Thus it is necessary to calculate the correlation function for lag times from nanoseconds to seconds. In our case the lag time resolution limit given by the TimeHarp 200 board is 100 ns. The calculation of the correlation function with lag time resolution 100 ns means 10 millions of multiplications for each lag time and every second of the measurement. Even for today's computers this task takes several times longer than the measurement itself.

The first FCS instruments solved this problem by using dedicated hardware correlators. The hardware correlator uses multiple sampling and delay times with quasi-logarithmic time scales[84, 85]. Our Confocor 1 also uses hardware correlator board ALV-500E (ALV Laser, Langen, Germany). The big disadvantage of the hardware correlators is that they do not keep the full resolution intensity trace. No offline analysis is thus possible, leading for example to problems with measurement distortions caused by intense bursts originating from rare unwanted aggregates. Another limitation of the hardware correlators is that they accept only the binary intensity – 1 or 0, depending on whether the photon was at the given time detected or not. As was shown in the theoretical introduction to TR-FCS, the analysis requires weighting of the individual photons entering the correlation function calculation, to insert the photon intensity as a real number (float or double precision).

The software correlation of the TTTR data implemented in the commercial programs was very slow, the programs did not allow FCS curve fitting and mainly the Time-Resolved FCS option was not included at all. It has to be mentioned that the TR-FCS data analysis, as a very young method, cannot be obtained commercially even today. These circumstances led to the development of own fast software correlation algorithms written in C (Dev-C++, Bloodshed software) together with graphical user interfaces in Origin (OriginPro70, OriginLab Corporation, Northampton, USA).

The correlation algorithm development happened in several steps. The first step was a simple fast correlation of TTTR data utilizing fixed switch between histogramming and multiplying, based on the idea of Magatti[86]. Already this algorithm was very fast, outrunning those days' commercial ones in speed by orders of magnitude. The calculation time depended on the square of the overall intensity and for a standard measurement the calculation time was one tenth of the measurement time, clearly suggesting a possible use of the algorithm in online software correlators.

Demands posed by the new ways of data analysis (photon weighting used in TR-FCS, experimental ACF weighting, markers from Z-scan, detectors routing in multi-focus setup) together with an inspiration taken from the newly appeared articles[87, 88] resulted in a much more variable algorithm, keeping still the calculation time much shorter than the measurement time. The basic principle is outlined in the next section. We have not published this algorithm yet, but recently a similar one was independently published by group of Seidel[88].

3.3.1 Basic principle of the correlation algorithm

1) In order to get the semi-logarithmic scaling of lag-times, let's assume that the autocorrelation function can be stored in a following table:

1	2	3	4	5	6	7	8	9	10	11	12	13	14	15	16
								9	10	11	12	13	14	15	16
								9	10	11	12	13	14	15	16
								9	10	11	12	13	14	15	16
								9	10	11	12	13	14	15	16
								9	10	11	12	13	14	15	16
								9	10	11	12	13	14	15	16
								9	10	11	12	13	14	15	16
								.							
								.							
								.							
								.							

Each number in a cell represents a particular lag-time τ that can be calculated as:

$$\tau = i \cdot 2^{j-1} \tau_{res}$$

where τ_{res} is the shortest lag-time, limited by the resolution of the TimeHarp 200 board (100 ns in our case). j is the row number ($j = 1,2,\ldots j_{max}$), i is the column number ($i = 1,2,..16$ for $j = 1$ and $i = 9, 10,\ldots 16$ for $j > 1$; see the table).

Let $P[i,j]$ be the temporal not-normalized autocorrelation function. At the beginning $P[i,j] = 0$ for every i, j.

j_{max} can be estimated from the measurement time T as it has to fulfill the following requirement: $2^{j_{max}-1} \cdot \tau_{res}.17 = T$ (If the measurement is longer we set $j_{max} = 35$).

2) Let all the photon events be registered in sets of the following table-like data structures:

t_0	t_1	t_2	t_3	t_4	t_5	t_6									. . .
I_{A0}	I_{A1}	I_{A2}	I_{A3}	I_{A4}	I_{A5}	I_{A6}									. . .
I_{B0}	I_{B1}	I_{B2}	I_{B3}	I_{B4}	I_{B5}	I_{B6}									. . .
c															

t_0, $t_1 \ldots t_{255}$ are the photon arrival times in numbers of τ_{res} (long long integer). I_{A0}, $I_{A1} \ldots I_{A255}$ and I_{B0}, $I_{B1} \ldots I_{B255}$ are intensities of arriving photons in the detector A and B, respectively, i.e. it is the number of photon events that occurred at time t_i during τ_{res} (in the case of an experiment and in the highest resolution, all intensities are equal 1, in the case of simulation and at lower resolution they can become any integer, in the case of time-resolved FCS experiment, it may be a real number (double precision); the number of columns can be smaller, but 16 at least. In the case of autocorrelation, intensities in both detectors equal.

Consecutive photon events are registered one by one. When the last column is used, the following event is going to be written again into the first column. (The number of detected photons is stored in the cell "counter" ("c"). Performing char(c), an integer from 0 to 255 indicating the storage column is obtained, which easily enables the circular data storing.

3) The data structure given above is used for the highest resolution data storage. For the sake of the resolution decrease, expected by the semi-logarithmic scaling, the set of such structures is used (36 in our case). The final scheme is then:

t_{0j}	t_{1j}	t_{2j}	t_{3j}	t_{4j}	t_{5j}	t_{6j}									. . .
I_{A0j}	I_{A1j}	I_{A2j}	I_{A3j}	I_{A4j}	I_{A5j}	I_{A6j}									. . .
I_{B0j}	I_{B1j}	I_{B2j}	I_{B3j}	I_{B4j}	I_{B5j}	I_{B6j}									. . .
c_j															

j is the resolution level, j = 1,2,3...36. At the beginning, all cells in all data structures equal zero.

4) The general algorithm for the nth photon event will be shown. First, lets introduce two more vectors: $I_{\text{direct}}(\tau)$ and $I_{\text{delayed}}(\tau)$, (τ is the lag-time) which will be used for asymmetric normalization of the final autocorrelation function. At the beginning, both equal zero.

   i) The photon is written into the char(c_1)th column of the 1st data structure, i.e. its arrival time and intensity.

   ii) $c_1 = c_1 + 1$

   iii) We look for the events that occurred at t_{m1}, so that $0 < t_{n1} - t_{m1} \leq 16$, (n = char($c_1$-1), m = char($c_1$-1-p)), p > 0.

   iv) All the events that fulfill the inequality given in iii) are correlated: $P[t_{n1} - t_{m1},1] = P[t_{n1} - t_{m1},1] + I_{An1} I_{Bm1}$ (in the following, subscripts A and B will be omitted for the sake of simplification). Additionally, the events are written into the normalization vectors: $I_{\text{direct}}[t_{n1} - t_{m1}] = I_{\text{direct}}[t_{n1} - t_{m1}] + I_{m1}$ and $I_{\text{delayed}}[t_{n1} - t_{m1}] = I_{\text{delayed}}[t_{n1} - t_{m1}] + I_{n1}$

   v) The resolution of the nth photon arrival time is decreased by factor 2, i.e. the photon is written into the second data structure with the arrival time $t_{\text{char(c2)2}}$:

$$t_{\text{char}(c_2)2} = \left\lfloor \frac{t_{n1}}{2} \right\rfloor .$$

   vi) If there is already a photon with the same arrival time, i.e. $t_{\text{char}(c_2)2} = t_{\text{char}(c_2-1)2}$, then $I_{\text{char}(c_2-1)2} = I_{\text{char}(c_2-1)2} + I_{n1}$. In this case, the procedure for the nth photon ends and the (n+1)th photon is taken into the correlation process.

   vii) If $t_{\text{char}(c_2)2} > t_{\text{char}(c_2-1)2}$, the photon, written in the char(c_2)th column of the second data structure, is left until it becomes "closed" (see further) and $c_2 = c_2 + 1$.

viii) The photon written in the previous column is "closed" at this moment, which means, no other photon from the previous data structure can contribute to its overall intensity. Thus, this photon, written in the char(c_2-2)th column of the second data structure, is taken for the further correlation: (n = char(c_2-2), m = char(c_2-2-p), p > 0), we look for all events that occurred at t_{m2} and fulfill the following inequality: $8 \le t_{n2} - t_{m2} \le 16$.

ix) Analogically to the highest resolution case, the events fulfilling viii) are correlated: $P[t_{n2} - t_{m2}, 2] = P[t_{n2} - t_{m2}, 2] + I_{n2} I_{m2}$ and the normalization vectors are incremented: $I_{\text{direct}}[t_{n2} - t_{m2}] = I_{\text{direct}}[t_{n2} - t_{m2}] + I_{m2}$ and $I_{\text{delayed}}[t_{n2} - t_{m2}] = I_{\text{delayed}}[t_{n2} - t_{m2}] + I_{n2}$.

x) Resolution of the arrival time of the photon correlated at the second resolution level is again factor 2 lowered and written to the char(c_3)th position of the third data structure and the steps iv) – x) are repeated for the following resolution level.

5) Generally, for the kth photon coming into the jth data structure (j > 1):

i) The photon is written to the char(c_j)th column of the j^{th} data structure with arrival time $t_{\text{char(cj)j}}$.

ii) If $t_{\text{char}(c_j)j} = t_{\text{char}(c_j-1)j}$, then $I_{\text{char}(c_j-1)j} = I_{\text{char}(c_j-1)j} + I_{\text{char}(c_{j-1}-2)j-1}$ and the new photon is taken to the first data structure.

iii) If $t_{\text{char}(c_j)j} > t_{\text{char}(c_j-1)j}$, then $c_j = c_j + 1$ and the photon written at the char(c_j-2)th position is taken to the correlation.

iv) n = char(cj-2), m = char(cj-2-p), p > 0, for all events that fulfill: $8 \le t_{nj} - t_{mj} \le 16$, the correlation curve and normalization vectors are restored: $P[t_{nj} - t_{mj}, j] = P[t_{nj} - t_{mj}, j] + I_{nj} I_{mj}$,

$I_{\text{direct}}[t_{nj} - t_{mj}] = I_{\text{direct}}[t_{nj} - t_{mj}] + I_{mj}$, $I_{\text{delayed}}[t_{nj} - t_{mj}] = I_{\text{delayed}}[t_{nj} - t_{mj}] + I_{nj}$.

v) The resolution of the arrival time $t_{\text{char(cj)j}}$ is two times decreased $t_{\text{char}(c_{j+1})j+1} = \left\lfloor \frac{t_{\text{char}(c_{j-2})j}}{2} \right\rfloor$ and the photon is shifted into the following structure.

6) To get the final normalized autocorrelation function – $G[\tau]$, $P[\tau(i,j)]$ as well as the normalization vectors $I_{\text{direct}}[\tau]$ and $I_{\text{delayed}}[\tau]$ need to be divided by the number of possible realization of the appropriate mathematical operation (i.e. multiplications for

$P[\tau(i,j)]$ and summarization for normalization vectors; for the sake of speed, this algorithm does not perform the operations at the times when no event occurred) N_c, used at the particular resolution and the particular lag-time: $N_c = \frac{T}{\tau_{res}} - \frac{\tau}{\tau_{res}}$, T is the measurement time.

The resulting autocorrelation function equals:

$$G[\tau] = \frac{P[\tau(i,j)] \cdot \left(\frac{T}{\tau_{res}} - \frac{\tau}{\tau_{res}} \right)}{I_{direct}[\tau] \cdot I_{delayed}[\tau]}$$

3.4 Z-scan automation

The first Z-scan measurements were performed fully manually, because the Confocor 1 software doesn't enable the required automation of focus movement in z-direction alternated with FCS data acquisition. After every FCS data acquisition at one z-position, the objective had to be manually shifted and a new data acquisition started, which was of course very inconvenient. First step towards the full automation was the introduction of a new sample holder, containing software controlled linear actuator (M-230.10, Mercury II Controller C-862, NetMove420 software, Physik Instrument GmbH & Co. Karlsruhe, Germany). The scheme of the innovated sample holder is in the Figure 22. Apart from the linear actuator the new setup includes three experimentally important features – an optimized flushing system, an immersion stirrer and mainly a temperature control of both the cuvette and the objective. The temperature control is used not only to keep a constant temperature during experiments, but also it enables performing measurements of the temperature dependence of the diffusion coefficient.

The automatic change of the sample position was manually time-synchronized with FCS data acquisition, thus allowing automatic measurement of the whole Z-scan experiment.

The full automation became possible only after the upgrade of the Confocor 1 by TimeHarp 200 board. Before and after a position change the linear actuator sends logical TTL signal that is registered by TimeHarp 200 board via its sub-D connector and inserted into TTTR data as a marker. The whole Z-scan experiment is thus saved into one TTTR data file with inserted markers, which enable to cut the measurement into pieces according to individual z-positions (Figure 23-upper graph).

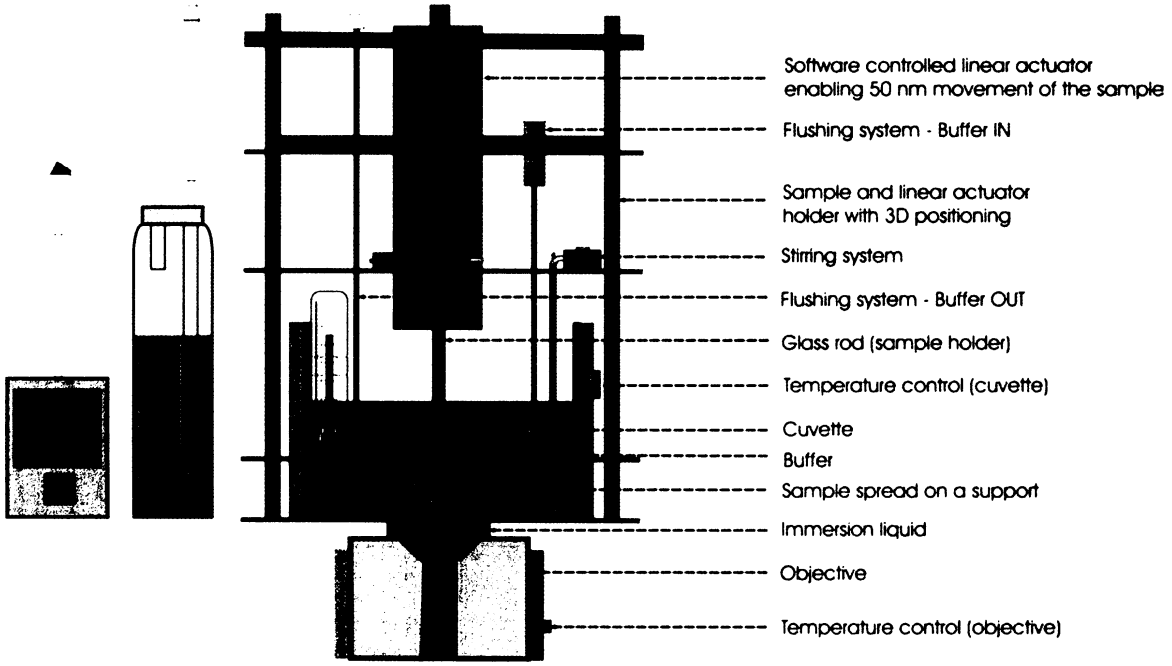

Figure 22. Scheme of sample holder for automatic Z-scan measurements with temperature control

3.5 Monte-Carlo simulations

As can be seen from the theoretical introduction to TR-FCS, the mathematics behind it is rather complicated and difficult to imagine, especially the negative "intensity" of weighted photons entering the correlation calculations. To prove the concept of TR-FCS, to test the developed correlation algorithms and the graphical user interfaces Monte-Carlo simulations based on real experiments were performed.

The basic concept of the simulations was taken from Wohland[89], although some important changes needed for successful simulation of TR-FCS experiment were made. The conditions for the computer simulations were as close as possible to the conditions used in the real membrane experiments described in the chapter 2.1. To simulate the fluorescence intensity signals arising from a confocal volume, in the middle of which 2-dimensional planar system (lipid membrane) oriented perpendicular to the optical z-axis is placed, a certain number of particles is included in a square of 4-μm side. We used from 10 to 800 particles corresponding to surface concentrations about 1 to 83 fmol/m^2. The center of the square is illuminated by a focused laser beam of wavelength 514.5 nm, giving diffraction limited illuminated area with a Gaussian intensity profile I(r) of radius w_0 261.5 nm:

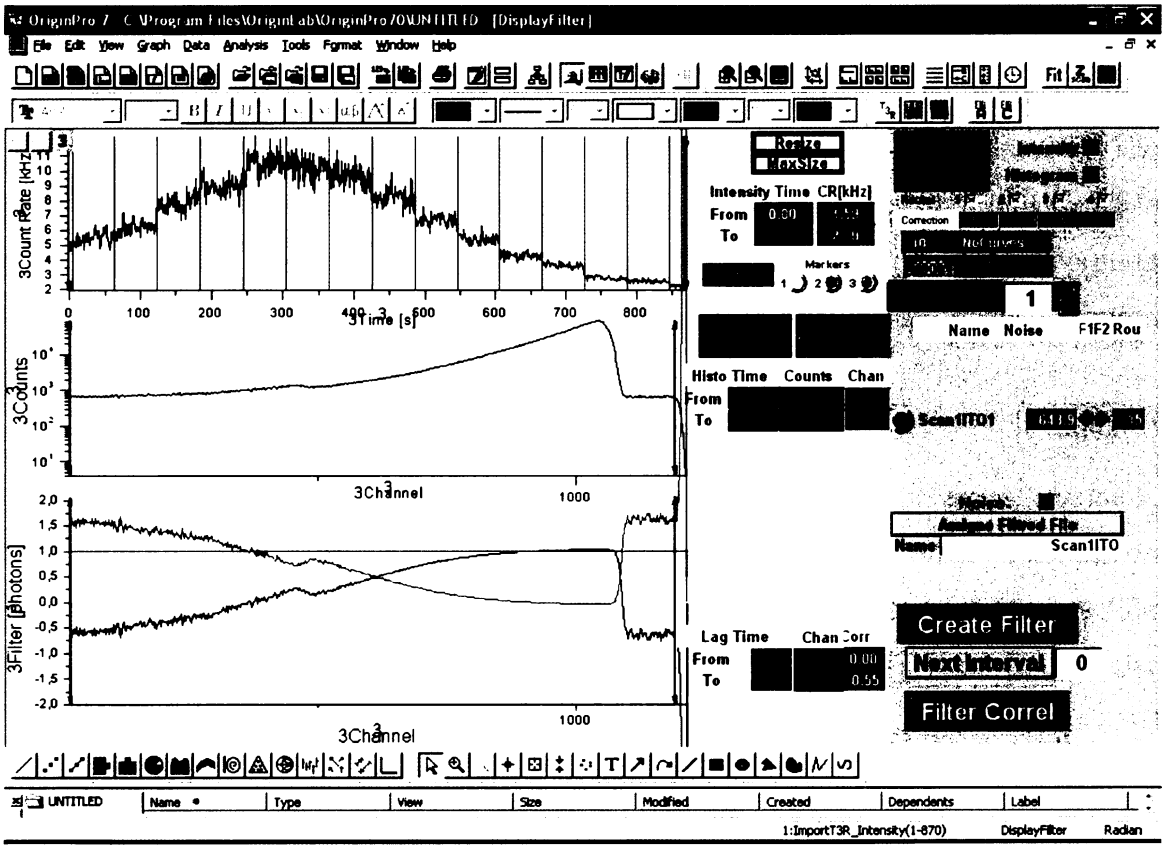

Figure 23. Snapshot of the OriginPro7 macro used for TR-FCS data analysis

$$I(\mathbf{r}) = 2Pe^{-|\mathbf{r}|^2/w_0^2} \tag{25}$$

where P is the power of the laser beam (100 μW). As the pinhole by spatial filtering ensures that only light close to the focal plane is collected, it doesn't influence the molecular detection function in our system. Each particle was considered to perform a random walk independently from the other particles. The time steps of the simulation were set to Δ_t = 100 ns corresponding to the smallest sampling time of the TimeHarp 200 board. The jump distance of a particle during that time step in each direction (x and y) was determined by a random variable with a Gaussian distribution with center value 0 and a standard deviation σ depending on the chosen diffusion coefficient D:

$$\sigma = \sqrt{2D\Delta_t} \tag{26}$$

The direction of the movement was completely random. At the start of the simulations, a random, uniform distribution of the particles was created inside the square. When a particle left the square after diffusion, a new particle was randomly created on the borders of the square, thus keeping the number concentration inside the square constant. Note that the number of particles in the illuminated area, which is much smaller than the simulated square, still fluctuates freely.

We neglect saturation and photobleaching effects in the simulations. Furthermore, we do not take into account possible intersystem crossing into triplet state or any other processes influencing fluorescence properties of the molecules. The number N_d of emitted photons for each particle at every simulation step thus depends only on the laser intensity at the actual position of the particle $I(\mathrm{r})$, on its absorption cross section ε, on its fluorescence quantum yield q_d, on the instrument detection efficiency q_i and the time step of the simulation Δ_t:

$$N_d = \mathrm{P}(I(\mathbf{r}) \cdot \Delta_t \cdot \varepsilon \cdot q_d \cdot q_i) \tag{27}$$

where $\mathrm{P}(x)$ is a random variable following a Poisson distribution with average value x. The random variable ensures that the detected photon counts follow a Poisson distribution as predicted for a stationary light source. The laser power and the detection efficiency were adjusted to get average brightness per molecule per second on the order of 10 kHz, a value similar to real experiments.

The next step of the simulation, similar to the TTTR data acquisition, is to generate for each photon a time of its detection after the excitation pulse. We assume an ideal delta function shape of the overall instrument response function. The photon detection time is then generated as a random variable with exponential distribution with the average value equal to molecule's lifetime. The detection time is then assigned a channel number by rounding to 39 ps resolution (the resolution of our MicroTime 200 board).

The final step of the simulation is saving of the generated photons in TTTR data format. When simulating multiple species experiments (up to 4), the photon origin is saved in the routing bits (similar to using multiple detectors setup).

For TR-FCS testing simulations, mixture of two non-interacting fluorescence species was used. They differed in the diffusion coefficient and in the excited state lifetime, their overall brightness was the same. The generated data were treated in the following way. First, histograms and autocorrelation functions of both species were calculated using routing information identifying the origin of every photon. Second, using the histograms of both species and the histogram of the mixture, filters for TR-FCS analysis were calculated. Third, using the filters autocorrelation functions of both species from the mixture were calculated discarding the routing information. Finally, both kinds of autocorrelation functions, routed and filtered, were compared. The result is shown in the Figure 24.

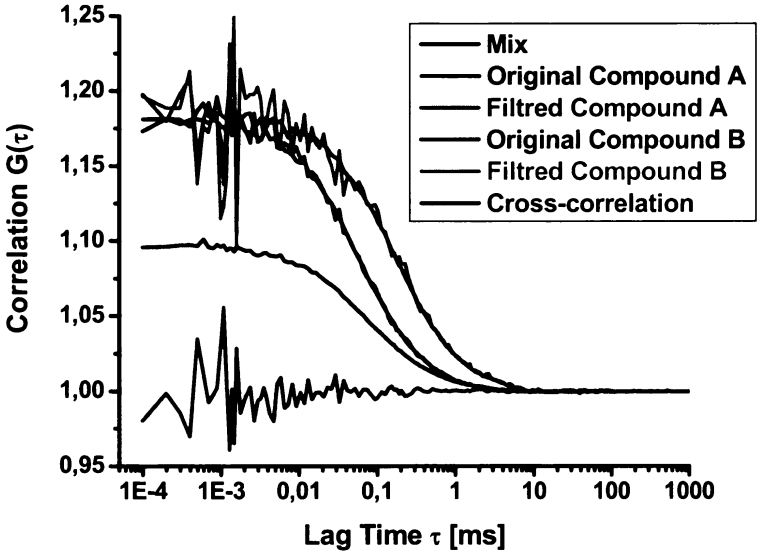

Figure 24. Monte-Carlo simulation of TR-FCS experiment

The comparison of the ACFs clearly shows that the filtered ACF is totally overlapping with the routed ACF, only the filtered one is noisier, which inherently comes from the statistical nature of its calculation. By this we proved that the concept of TR-FCS and our software for TR-FCS data analysis work.

Monte-Carlo simulations are very attractive for FCS field, as they can help judging correctness of ideas and they also may give a hint where the problem is not soluble analytically. Presently we are improving the performance of the simulations (speed) and focusing on measuring diffusion of molecules whose size is comparable with the confocal detection volume, for example large unilamellar vesicles (LUVs) or DNA.

3.6 Experimental testing

After *in silico* testing of TR-FCS, we performed two simple tests of the method by real experiments.

First we tested the ability of TR-FCS to separate the autocorrelation curves of dyes with similar diffusion coefficients, but with different lifetimes and thus simultaneously track their concentration in a mixture. As a model system we have chosen a mixture of two non-interacting dyes in methanol: BODIPY630 (BODIPY® 630/650-X, STP ester) with a lifetime of 4.4 ns, and DiD (1,1'-dioctadecyl- 3,3,3',3' tetramethyl-indodicarbocyanine perchlorate) with a lifetime of 0.9 ns. First, the solutions of pure dyes were measured, then in five steps a small amount of concentrated

BODIPY630 solution was added to the DiD stock solution and TR-FCS was applied to separate the ACFs.

The results are shown in the Figure 25. The TR-FCS analysis has fully preserved the shapes of the respective single ACFs, giving the same diffusion time resolution as for single species, and it has precisely determined concentrations of both species.

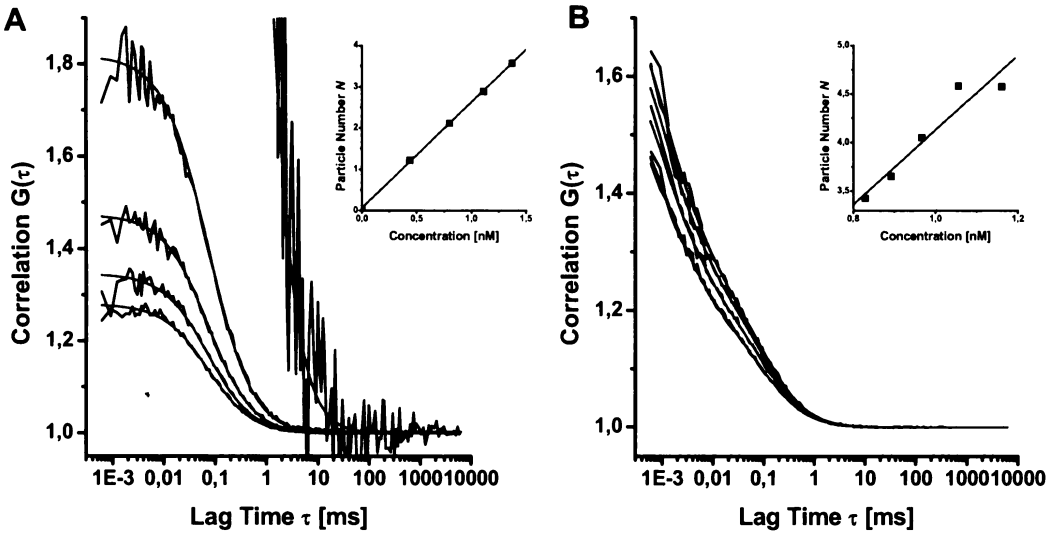

Figure 25. To the methanol solution of DiD, small amounts of concentrated methanol solution of BODIPY630 were gradually added. (a) The amplitude of separated autocorrelation curve of BODIPY630 decreases, which means an increase of the concentration (see the inlet graph). (b) The separated autocorrelation curve of DiD show gradually increasing amplitude (i.e. decrease of concentration) caused by dilution of the DiD stock solution by BODIPY630 addition. DiD in methanol show cis-trans isomerisation, hence the fast initial decay of these FCS curves.

In the second experiment we tested the utility of TR-FCS approach for obtaining the cross-correlation function in a single-channel measurement. The model system consisted of independently prepared large unilamellar vesicles (LUVs) labeled with water-insoluble DiD lipid tracer and small unilamellar vesicles (SUVs) labeled with partially water-soluble BODIPY630 dye. When the solutions were mixed, the partially water-soluble BODIPY630 dye contaminated the DiD labeled LUVs, while the water insoluble DiD molecules were expected to remain in LUVs. Results of TR-FCS analysis, the separated autocorrelation curves of the components, as well as their calculated cross-correlation, are presented in Figure 26. The cross-correlation function indicates a presence of doubly labeled species, which are in our case the DiD labeled LUVs contaminated with the water soluble BODIPY630 dye. In case of non-interacting

single labeled species, the cross-correlation function would have constant amplitude equal to 1.

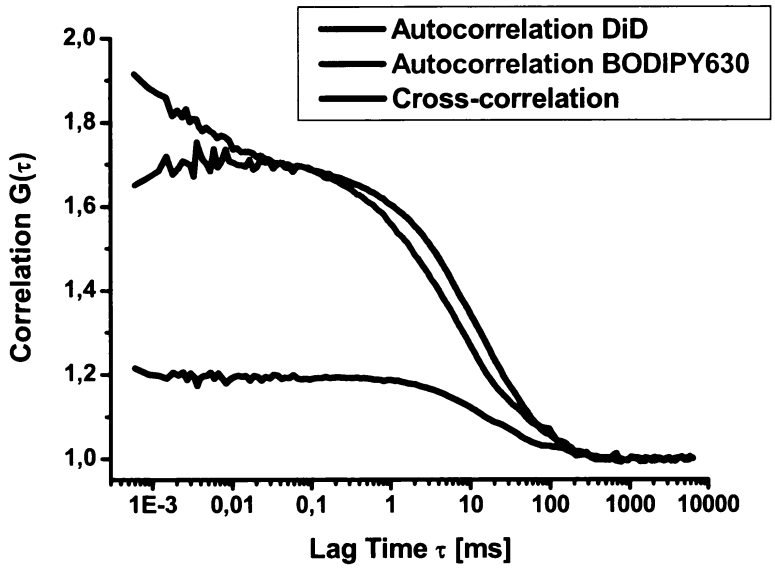

Figure 26. Auto- and cross-correlation functions of components in a vesicle mixture. LUVs were labeled with water-insoluble DiD, whereas SUVs were labeled with water-soluble BODIPY630. The significant amplitude of the cross-correlation function is caused by the interchange of water-soluble BODIPY630 molecules between the two kinds of vesicles.

3.7 Applications (Paper XI, Paper XIV)

The basic application of the presented hardware and software upgrade are simultaneous TCSPC and FCS experiments. Interpretation of FCS data alone is often tedious and requires additional experiments. Having simultaneously the lifetime information can help a lot in this situation. For example the excited state decay pattern gives direct information on the amount of non-correlated background light or reflected and Raman scattered light. It may identify impurities in solutions or reveal whether the studied fluorophore changes its lifetime during the FCS experiment.

In Paper XI we exploit the lifetime added value of the upgraded Confocor 1 setup together with the optimized sample holder (Figure 22) for studying the nanoscale-confined diffusion of fluorescent probe molecules inside highly ordered alumina nanopores. The motivation was to restrict the 3D diffusion of studied molecules by the nanopores and thus reach the apparent 1D diffusion leading to longer observation times of the molecules. The ACF analysis really revealed the apparent 1D diffusion inside the

pores with a dwell time in the confocal volume up to 19 times longer than in the case of the bulk 3D diffusion. Moreover the apparent concentration was lowered due to a smaller effective probe volume. Analyzing the fluorescence lifetime changes in the nanostructure, we found that no collisional quenching of fluorescence at the pore walls occurs. Our findings render one-dimensional fluorescence fluctuation spectroscopy (1DFCS) in ordered nanoporous alumina an efficient tool to study macromolecules in channel-type confinement and to evaluate the performance of these membranes in separation and sensing.

The simultaneous TCSPC and FCS experiments appeared to be very helpful in DNA condensation studies. The task of these studies is to find an efficient DNA condensing agent for application in non-viral gene therapy (NVGT). The condensing agent is supposed to effectively pack large DNA molecules into so-called nanoparticles, deliver them into targeted cells and enable the cell transfection.

We concentrated on the first part of the NVGT, the efficient condensation of DNA molecules. We have shown that FCS is a suitable tool for testing condensers efficiency[90-92, Paper XII, Paper XIII]. The FCS data monitoring the condensation process are complicated and not still fully understood. The problems arise from the starting size of DNA molecule, which is larger than the focal volume, from its complicated conformation in the non-condensed form, and from the DNA fluorescent labeling usually performed by intercalating dyes, which are partially expelled from the double coil during the condensation process.

The combined TCSPC and FCS have substantially contributed to the data interpretation by the ability to distinguish between a dye release and a dye quenching[Paper XIV]. When the overall intensity goes down and the excited state lifetime remains constant, we observe dye release. As soon as the excited state lifetime is shortened proportionally to the intensity decrease, no dye release happens; only the environment of the intercalated dye in DNA strand is changing, leading to a decrease of the quantum yield of the dye.

Among advanced options of the presented upgrade belong applications of TR-FCS. Two of them, using multiple labeling, were sketched out in the previous section. Another simple, but useful, application of TR-FCS is a removal of detector afterpulsing from ACF[24]. However, the main power of the method lies in systems, where we study kinetics connected with a lifetime change of fluorophore. For example one can study rate constants of the opening and closing of the double-stranded terminal segments of

cTAR[93] by introducing a fluorescence label to one end of the cTAR and a fluorescence quencher to the second end (so called beacon). As the cTAR is opening and closing, the lifetime of the fluorophore is changing and the TR-FCS should be able to study its kinetics. This work is currently under progress.

Another already worked out application of TR-FCS is described in the next chapter.

Chapter 4 TR-FCS combined with lifetime tuning (Paper III)

4.1 General introduction - surface sensitive fluorescence techniques

In cell and molecular biology, a large number of molecular events in cellular surfaces such as cell adhesion, binding of cells by hormones, secretion of neurotransmitters, and membrane dynamics have been studied with conventional fluorescence microscopes. However, fluorophores that are bound to the specimen surface and those in the surrounding medium exist in an equilibrium state. When these molecules are excited and detected with a conventional (confocal or wide-field) fluorescence microscope, the resulting fluorescence from those fluorophores bound to the surface is often undistinguishable from the "background" fluorescence of unbound molecules.

There are two basic solutions, to suppress the fluorescence of unbound molecule or to discern between fluorescence emitted by bound and unbound molecules, both of which require bringing the studied system, a living cell membrane or its model (e.g. SPBs), close to an optical interface (e.g. glass-water).

To suppress the unbound molecule fluorescence, the total internal reflection fluorescence microscopy (TIRFM) can be used. When light propagates within an optically dense medium (e.g. quartz or glass) and hits an interface with a less optically dense medium (e.g. aqueous solution) at the angle larger than the critical angle, a total internal reflection appears. Although the light is fully reflected, an evanescent field is generated that extends beyond the interface into the less dense medium. The evanescent electromagnetic field decays exponentially from the interface and the penetration depth (the thickness of the evanescent field) depends on the wavelength of the light, the incidence angle and the refractive indices of the media, and is in the range of 100 to 200 nm for visible light and standard interface (quartz or glass - water). The evanescent field provides the surface selectivity of TIRFM. Only fluorophores adsorbed, adhered, or bound to the surface are excited and therefore fluoresce. Conversely, fluorophores in bulk solution are not excited. Therefore, if the surface is made biologically active so that one may 'trap' fluorescently-labeled compounds of interest, one can detect analytes within complex sample solutions.

Apart from simple imaging, TIRFM is used in combination with fluorescence recovery after photobleaching (FRAP)[78, 94] and FCS[95-97] to study dynamics of membrane bound molecules, which are in equilibrium with free molecules in solution.

To discern between the fluorescence of bound and unbound molecules, we use another electromagnetic effect caused by an optical interface between two media. The fluorescent molecule can be assumed to be a point-like oscillating dipole. The radiative emission of such a dipole is influenced by optical properties of its surroundings. For example the radiative emission rate (related to the fluorescence lifetime) depends on the refractive index of the medium and also on the presence of any nearby optical interface. In other words, fluorescent molecules in optically homogeneous bulk medium far way (units of emission wavelength) from any optical interface have different lifetime than molecules close to such an interface[98-100]. The relative change of the fluorescent lifetime depends on the optical properties of the interface, on the orientation and the quantum yield of the dye and on the distance between the dye and the interface. The interface is usually created by a solid material (surface) and water solution. For light absorbing surfaces (semiconductors and conductors) the shortening of the lifetime is very efficient, exhibiting a cubic dependence for short distances[101] with the effective radius (a decrease to half lifetime) on the order of tens of nanometers. Recent articles offer full theoretical description not only of the lifetime changes, but also of the intensity modulation by optical interfaces[99, 100, 102-105].

Whereas the intensity modulation is used in fluorescence interference contrast microscopy[104, 105] for measuring distances of the labeled species from the supporting surface, we exploit the fluorescence lifetime change for discerning between fluorescence from the bound and free molecules. The presented lifetime tuning can be used in fluorescence lifetime imaging microscopy (FLIM), or for dynamic point analysis using TR-FCS[Paper III].

4.2 Lifetime tuning within SPBs

Supported phospholipid bilayers are by default closely attached to the supporting surface – to the optical interface. Considering the thickness of the bilayer between 4-6 nm (depending on the lipid composition) and 1 nm thick water layer between SPBs and the surface, any fluorescent dye embedded in SPBs (labeled lipid or lipophilic molecule) is within a distance of several nanometers from the optical interface. It means

that its lifetime is influenced by the optical properties of the support – its complex refractive index for the emission wavelength.

The lifetime of dyes in the close vicinity of light-nonabsorbing supports (glass, quartz, mica - dielectrics) is only moderately modulated, resulting in unsuitability of these supports for further time-resolved applications. A totally different situation is obtained for semiconducting or metallic supports. These materials absorb visible light, a feature described by their non-zero imaginary refractive index, and this results in non-radiative energy transfer from the excited dye to the support. It means that the lifetime of the dye in SPBs on such supports is significantly shortened, leading to the possibility of differentiating between bound and free molecules.

In Paper III we show both theoretically and experimentally how much the lifetime of a dye is shortened in SPBs on different supports. Moreover, for selected supports (naturally oxidized silicon and glass covered with conductive indium-tin oxide layer (ITO)) we also inspect the distance dependence of the lifetime modulation (Figure 27). As the investigations found both of the studied systems suitable for resolving bound and free molecules (significant shortening of the lifetime close to the surface and steep distance dependence on the order of tens of nanometers), series of TR-FCS experiments aiming to resolve SPBs confined and free bulk diffusion of the same fluorophore were performed.

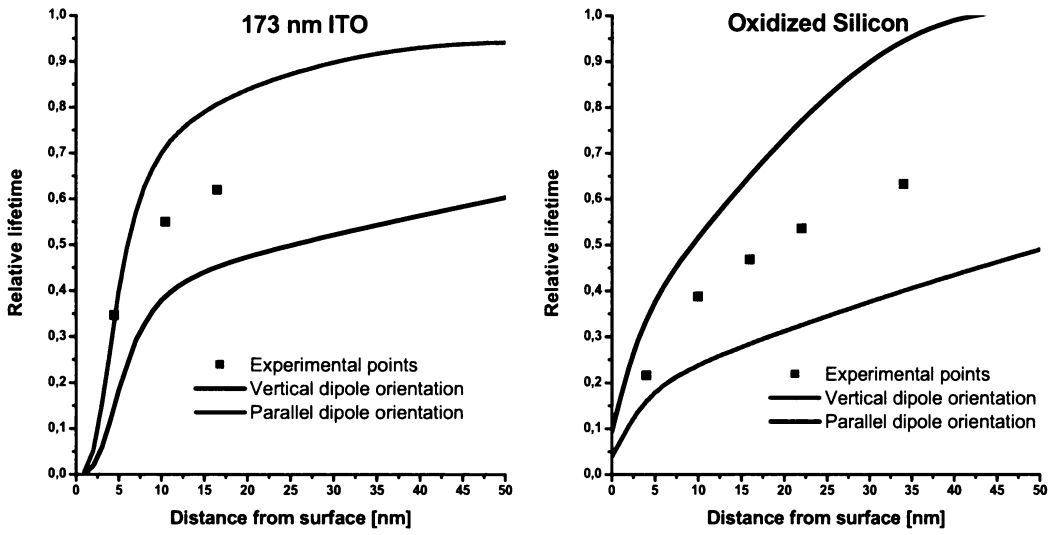

Figure 27. Theoretical and experimental dependence of relative lifetime of β-C8-BODIPY® 500/510 C5-HPC in lipid monolayer on its distance from surface of a) 173 nm thick ITO layer on glass b) naturally oxidized silicon. Shown are data for vertical (solid line) and parallel (dashed line) orientation of the dye dipole towards the surface and experimental points (squares).

The used testing system comprises SPBs on ITO (silicon) and SUVs in solution, both prepared from DOPC/DOPS 4/1 mixture labeled 1:100 000 with β-C8-BODIPY® 500/510 C5-HPC (Figure 28). We focused with the pulsed laser beam onto the interface and performed TTTR measurement where the fluorescence signal was originating from both SPBs and SUVs. The ACF calculated from these data by standard correlation is a superposition of both diffusive modes (within SPBs and SUVs in bulk) (black line in the Figure 29). Next step was TTTR measurement deep in the bulk faraway from any surface for obtaining pure SUVs signal and in the last step we flushed away SUVs by pure buffer and measured SPBs alone. We have thus obtained all fluorescence lifetime decays necessary for calculation of the filters needed for TR-FCS analysis. The TTTR data of the mixture were then analyzed using the calculated filters.

A simple comparison of the autocorrelation curves obtained for SPBs from the mixed SPB/vesicle systems with those obtained from the isolated planar lipid layers demonstrates the validity of the TR-FCS approach (green and red line in the Figure 29).

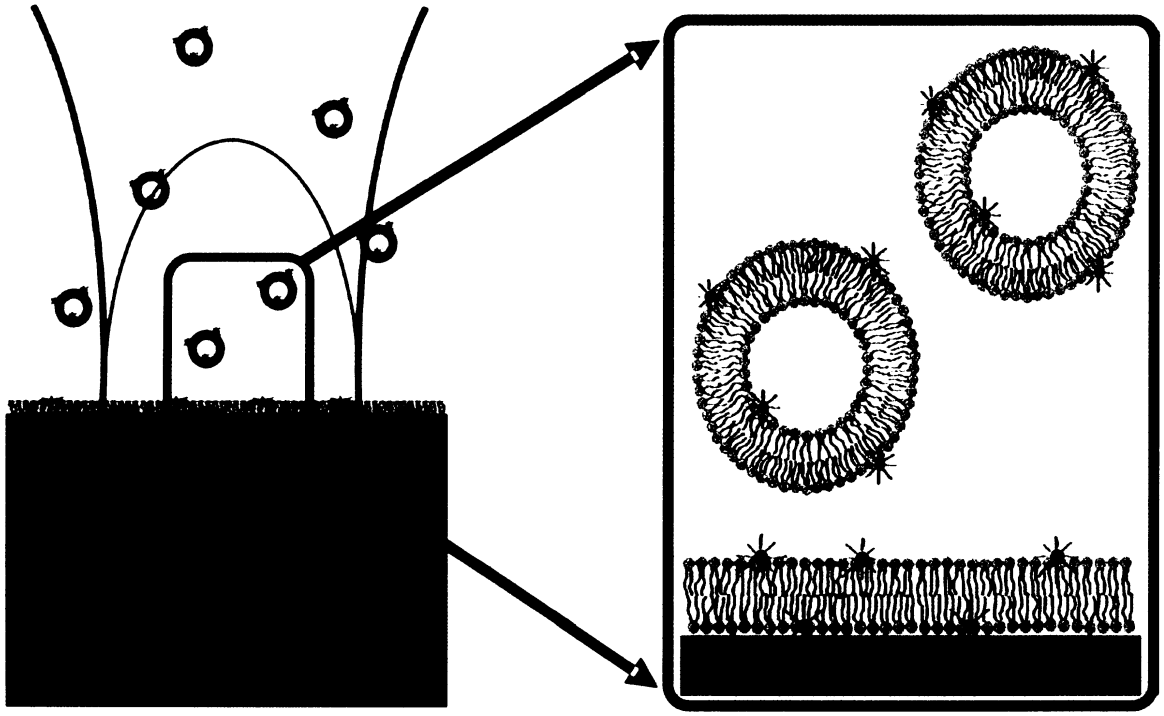

Figure 28. Illustration of a TR-FCS experiment for simultaneous characterization of 2 and 3 dimensional diffusion. The diameter of SUVs is 50 ± 10 nm, beam waist radius is 250 nm, and thickness of the bilayer is around 5 nm.

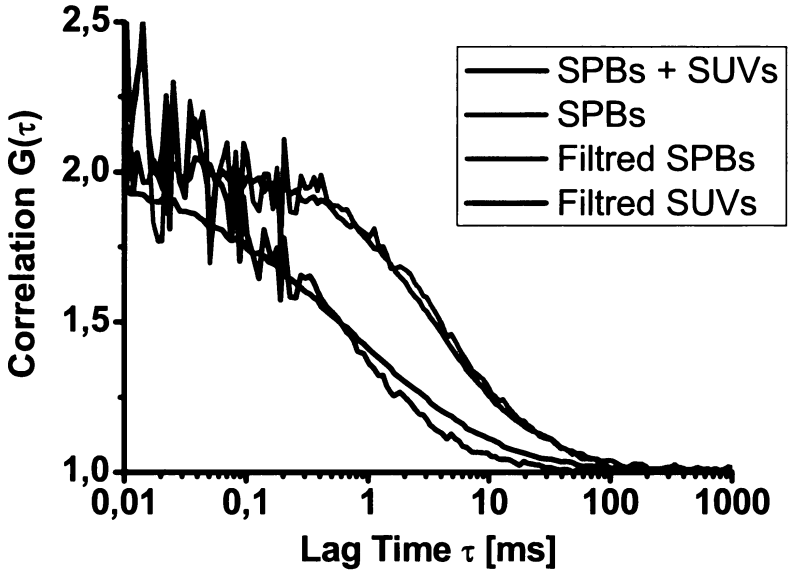

Figure 29. Comparison of normalized correlation curves for labeled lipid β-C8-BODIPY® 500/510 C5-HPC in DOPC/DOPS 4/1 SPBs on glass covered with 173 nm ITO and measured in buffer with and without SUVs using TR-FCS.

In the presented TR-FCS experiments the fluorescence decay histograms of all components in the mixture were obtained by independent measurements. In some cases this may not be possible, for example when the components exist in mutual equilibrium (e.g. lateral diffusion of weakly bound membrane proteins) or when they are physically inseparable (e.g. diffusion in the inner and the outer layer of SPBs). The solution to this problem is to fit the histogram of the measured mixture by the iterative convolution technique and to reconstruct the decay patterns of components by a convolution of the instrument response function (IRF) with the decay model of each component containing the fitted parameters. Although the suggested procedure is theoretically straightforward, its experimental realization is made difficult by anisotropy phenomenon and technical artifacts of the used detectors (IRF dependence on the overall intensity).

In conclusion, we have suggested and realized TR-FCS based method for resolving between the diffusion of SPBs bound and free fluorophore. The application of this new method is expected to be in the field of simultaneous characterization of 2-dimensional protein diffusion on SPBs and 3-dimensional protein diffusion in bulk. Moreover, cross-correlation analysis might give direct information on protein binding rates.

References

1. Magde, D.; Elson, E.; Webb, W. W., Thermodynamic fluctuations in a reacting system - measurement by fluorescence correlation spectroscopy. *Physical Review Letters* **1972,** 29, (11), 705-708.
2. Elson, E.; Magde, D., Fluorescence Correlation Spectroscopy. I.Conceptual Basis and Theory. *Biopolymers* **1974,** 13, 1-27.
3. Magde, D.; Elson, E., Fluorescence Correlation Spectroscopy. II.An Experimental Realization. *Biopolymers* **1974,** 13, 29-61.
4. Ehrenberg, M.; Rigler, R., Rotational Brownian-motion and fluorescence intensity fluctuations. *Chemical Physics* **1974,** 4, (3), 390-401.
5. Icenogle, R. D.; Elson, E. L., Fluorescence Correlation Spectroscopy and Photobleaching Recovery of Multiple Binding Reactions .1. Theory and Fcs Measurements. *Biopolymers* **1983,** 22, (8), 1919-1948.
6. Icenogle, R. D.; Elson, E. L., Fluorescence Correlation Spectroscopy and Photobleaching Recovery of Multiple Binding Reactions .2. Fpr and Fcs Measurements at Low and High DNA Concentrations. *Biopolymers* **1983,** 22, (8), 1949-1966.
7. Kask, P.; Piksarv, P.; Mets, U., Fluorescence Correlation Spectroscopy in the Nanosecond Time Range - Photon Antibunching in Dye Fluorescence. *European Biophysics Journal with Biophysics Letters* **1985,** 12, (3), 163-166.
8. Mets, U.; Widengren, J.; Rigler, R., Application of the antibunching in dye fluorescence: Measuring the excitation rates in solution. *Chemical Physics* **1997,** 218, (1-2), 191-198.
9. Rauer, B.; Neumann, E.; Widengren, J.; Rigler, R., Fluorescence correlation spectrometry of the interaction kinetics of tetramethylrhodamin alpha-bungarotoxin with Torpedo californica acetylcholine receptor. *Biophysical Chemistry* **1996,** 58, (1-2), 3-12.
10. Bonnet, G.; Krichevsky, O.; Libchaber, A., Kinetics of conformational fluctuations in DNA hairpin-loops. *Proceedings of the National Academy of Sciences of the United States of America* **1998,** 95, (15), 8602-8606.
11. Haupts, U.; Maiti, S.; Schwille, P.; Webb, W. W., Dynamics of fluorescence fluctuations in green fluorescent protein observed by fluorescence correlation spectroscopy. *Proceedings of the National Academy of Sciences of the United States of America* **1998,** 95, (23), 13573-13578.
12. Berland, K. M.; So, P. T. C.; Gratton, E., 2-Photon Fluorescence Correlation Spectroscopy - Method and Application to the Intracellular Environment. *Biophysical Journal* **1995,** 68, (2), 694-701.
13. Schwille, P.; MeyerAlmes, F. J.; Rigler, R., Dual-color fluorescence cross-correlation spectroscopy for multicomponent diffusional analysis in solution. *Biophysical Journal* **1997,** 72, (4), 1878-1886.
14. Böhmer, M.; Wahl, M.; Rahn, H. J.; Erdmann, R.; Enderlein, J., Time-resolved fluorescence correlation spectroscopy. *Chemical Physics Letters* **2002,** 353, (5-6), 439-445.
15. Rigler, R.; Mets, U.; Widengren, J.; Kask, P., Fluorescence correlation spectroscopy with high count rate and low background: analysis of translational diffusion. *European Biophysics Journal* **1993,** 22, 169-175.
16. Qian, H.; Elson, E. L., Analysis of Confocal Laser-Microscope Optics for 3-D Fluorescence Correlation Spectroscopy. *Applied Optics* **1991,** 30, (10), 1185-1195.

17. Enderlein, J.; Pampaloni, F., Unified operator approach for deriving Hermite-Gaussian and Laguerre-Gaussian laser modes. *Journal of the Optical Society of America a-Optics Image Science and Vision* **2004,** 21, (8), 1553-1558.
18. Sorscher, S. M.; Klein, M. P., Profile of a Focused Collimated Laser-Beam near the Focal Minimum Characterized by Fluorescence Correlation Spectroscopy. *Review of Scientific Instruments* **1980,** 51, (1), 98-102.
19. Enderlein, J., Theoretical study of detection of a dipole emitter through an objective with high numerical aperture. *Optics Letters* **2000,** 25, (9), 634-636.
20. Enderlein, J.; Gregor, I.; Patra, D.; Fitter, J., Art and artefacts of fluorescence correlation spectroscopy. *Current Pharmaceutical Biotechnology* **2004,** 5, (2), 155-161.
21. Gregor, I.; Patra, D.; Enderlein, J., Optical saturation in fluorescence correlation spectroscopy under continuous-wave and pulsed excitation. *Chemphyschem* **2005,** 6, (1), 164-170.
22. Widengren, J.; Mets, U.; Rigler, R., Fluorescence Correlation Spectroscopy of Triplet-States in Solution - a Theoretical and Experimental-Study. *Journal of Physical Chemistry* **1995,** 99, (36), 13368-13379.
23. Thompson, N. L., Fluorescence Correlation Spectroscopy. In *Topics in Fluorescence Spectroscopy*, Lakowicz, J. R., Ed. Plenum Press: New York, 1991; Vol. 1, pp 337-378.
24. Enderlein, J.; Gregor, I., Using fluorescence lifetime for discriminating detector afterpulsing in fluorescence-correlation spectroscopy. *Review of Scientific Instruments* **2005,** 76, (3), -.
25. Meseth, U.; Wohland, T.; Rigler, R.; Vogel, H., Resolution of fluorescence correlation measurements. *Biophysical Journal* **1999,** 76, (3), 1619-1631.
26. Enderlein, J.; Erdmann, R., Fast fitting of multi-exponential decay curves. *Optics Communications* **1997,** 134, (1-6), 371-378.
27. Rothen, A.; Landsteiner, K., Serological reactions of protein films and denaturated proteins. *Journal of Experimental Medicine* **1942,** 76, 437-450.
28. Cuypers, P. A.; Corsel, J. W.; Janssen, M. P.; Kop, J. M. M.; Hermens, W. T.; Hemker, H. C., The Adsorption of Prothrombin to Phosphatidylserine Multilayers Quantitated by Ellipsometry. *Journal of Biological Chemistry* **1983,** 258, (4), 2426-2431.
29. Corsel, J. W.; Willems, G. M.; Kop, J. M. M.; Cuypers, P. A.; Hermens, W. T., The Role of Intrinsic Binding Rate and Transport Rate in the Adsorption of Prothrombin, Albumin, and Fibrinogen to Phospholipid-Bilayers. *Journal of Colloid and Interface Science* **1986,** 111, (2), 544-554.
30. McCrackin, F. L.; Passaglia, E.; Stromberg, R. R.; Steinberg, H. L., Measurement of the Thickness and Refractive Index of Very Thin Films and the Optical Properties of Surfaces by Ellipsometry. *Journal of Research of the National Bureau of Standards, Section A: Physics and Chemistry* **1963,** 67A, (4), 363-377.
31. Azzam, R. M. A.; Bashara, N. M., *Ellipsometry and polarized light.* Elsevier: Amsterdam, 1977.
32. Charitat, T.; Bellet-Amalric, E.; Fragneto, G.; Graner, F., Adsorbed and free lipid bilayers at the solid-liquid interface. *European Physical Journal B* **1999,** 8, (4), 583-593.
33. Tamm, L. K.; Mcconnell, H. M., Supported Phospholipid-Bilayers. *Biophysical Journal* **1985,** 47, (1), 105-113.
34. Roberts, G., *Langmuir Blodgett Films.* Plenum Press: New York, 1990.

35. Grant, L. M.; Tiberg, F., Normal and lateral forces between lipid covered solids in solution: Correlation with layer packing and structure. *Biophysical Journal* **2002,** 82, (3), 1373-1385.
36. Heyse, S.; Ernst, O. P.; Dienes, Z.; Hofmann, K. P.; Vogel, H., Incorporation of rhodopsin in laterally structured supported membranes: Observation of transducin activation with spatially and time-resolved surface plasmon resonance. *Biochemistry* **1998,** 37, (2), 507-522.
37. McConnell, H. M.; Watts, T. H.; Weis, R. M.; Brian, A. A., Supported Planar Membranes in Studies of Cell-Cell Recognition in the Immune-System. *Biochimica Et Biophysica Acta* **1986,** 864, (1), 95-106.
38. Brian, A. A.; Mcconnell, H. M., Allogeneic Stimulation of Cyto-Toxic T-Cells by Supported Planar Membranes. *Proceedings of the National Academy of Sciences of the United States of America-Biological Sciences* **1984,** 81, (19), 6159-6163.
39. Srinivasan, M. P.; Ratto, T. V.; Stroeve, P.; Longo, M. L., Patterned supported bilayers on self-assembled monolayers: Confinement of adjacent mobile bilayers. *Langmuir* **2001,** 17, (25), 7951-7954.
40. Steinem, C.; Janshoff, A.; Ulrich, W. P.; Sieber, M.; Galla, H. J., Impedance analysis of supported lipid bilayer membranes: A scrutiny of different preparation techniques. *Biochimica Et Biophysica Acta-Biomembranes* **1996,** 1279, (2), 169-180.
41. Keller, C. A.; Glasmastar, K.; Zhdanov, V. P.; Kasemo, B., Formation of supported membranes from vesicles. *Physical Review Letters* **2000,** 84, (23), 5443-5446.
42. Starr, T. E.; Thompson, N. L., Formation and characterization of planar phospholipid bilayers supported on TiO2 and SrTiO3 single crystals. *Langmuir* **2000,** 16, (26), 10301-10308.
43. Baumgart, T.; Offenhausser, A., Polysaccharide-supported planar bilayer lipid model membranes. *Langmuir* **2003,** 19, (5), 1730-1737.
44. Richter, R. P.; Berat, R.; Brisson, A. R., Formation of solid-supported lipid bilayers: An integrated view. *Langmuir* **2006,** 22, (8), 3497-3505.
45. Richter, R. P.; Maury, N.; Brisson, A. R., On the effect of the solid support on the interleaflet distribution of lipids in supported lipid bilayers. *Langmuir* **2005,** 21, (1), 299-304.
46. Giesen, P. L. A.; Hemker, H. C.; Hermens, W. T., Production of Thrombin as a Probe for Mixing of Phospholipids in Membranes on Solid Supports. *Biochimica Et Biophysica Acta-Biomembranes* **1995,** 1237, (1), 43-48.
47. Richter, R. P.; Brisson, A., QCM-D on mica for parallel QCM-D-AFM studies. *Langmuir* **2004,** 20, (11), 4609-4613.
48. Richter, R.; Mukhopadhyay, A.; Brisson, A., Pathways of lipid vesicle deposition on solid surfaces: A combined QCM-D and AFM study. *Biophysical Journal* **2003,** 85, (5), 3035-3047.
49. Reviakine, I.; Brisson, A., Formation of supported phospholipid bilayers from unilamellar vesicles investigated by atomic force microscopy. *Langmuir* **2000,** 16, (4), 1806-1815.
50. McKiernan, A. E.; Ratto, T. V.; Longo, M. L., Domain growth, shapes, and topology in cationic lipid bilayers on mica by fluorescence and atomic force microscopy. *Biophysical Journal* **2000,** 79, (5), 2605-2615.
51. Ratto, T. V.; Longo, M. L., Obstructed Diffusion in Phase-Separated Supported Lipid Bilayers: A Combined Atomic Force Microscopy and Fluorescence Recovery after Photobleaching Approach. *Biophys. J.* **2002,** 83, (6), 3380-3392.

52. Richter, R. P.; Brisson, A., Characterization of lipid bilayers and protein assemblies supported on rough surfaces by atomic force microscopy. *Langmuir* **2003,** 19, (5), 1632-1640.
53. Reviakine, I.; Simon, A.; Brisson, A., Effect of Ca2+ on the morphology of mixed DPPC-DOPS supported phospholipid bilayers. *Langmuir* **2000,** 16, (4), 1473-1477.
54. Feng, Z. V.; Spurlin, T. A.; Gewirth, A. A., Direct visualization of asymmetric behavior in supported lipid bilayers at the gel-fluid phase transition. *Biophysical Journal* **2005,** 88, (3), 2154-2164.
55. Groves, J. T.; Dustin, M. L., Supported planar bilayers in studies on immune cell adhesion and communication. *Journal of Immunological Methods* **2003,** 278, (1-2), 19-32.
56. Cuypers, P. A.; Willems, G. M.; Kop, J. M. M.; Corsel, J. W.; Janssen, M. P.; Hermens, W. T., Kinetics of Protein Sorption on Phospholipid-Membranes Measured by Ellipsometry. *Acs Symposium Series* **1987,** 343, 208-221.
57. Reviakine, I.; Bergsma-Schutter, W.; Mazeres-Dubut, C.; Govorukhina, N.; Brisson, A., Surface topography of the p3 and p6 annexin V crystal forms determined by atomic force microscopy. *Journal of Structural Biology* **2000,** 131, (3), 234-239.
58. Reviakine, I.; Bergsma-Schutter, W.; Brisson, A., Growth of protein 2-d crystals on supported planar lipid bilayers imaged in situ by AFM. *Journal of Structural Biology* **1998,** 121, (3), 356-362.
59. Grandbois, M.; Clausen-Schaumann, H.; Gaub, H., Atomic force microscope imaging of phospholipid bilayer degradation by phospholipase A(2). *Biophysical Journal* **1998,** 74, (5), 2398-2404.
60. Milon, S.; Hovius, R.; Vogel, H.; Wohland, T., Factors influencing fluorescence correlation spectroscopy measurements on membranes: simulations and experiments. *Chemical Physics* **2003,** 288, (2-3), 171-186.
61. Hess, S. T.; Webb, W. W., Focal volume optics and experimental artifacts in confocal fluorescence correlation spectroscopy. *Biophysical Journal* **2002,** 83, (4), 2300-2317.
62. Korlach, J.; Schwille, P.; Webb, W. W.; Feigenson, G. W., Characterization of lipid bilayer phases by confocal microscopy and fluorescence correlation spectroscopy. *Proceedings of the National Academy of Sciences of the United States of America* **1999,** 96, (15), 8461-8466.
63. Schwille, P.; Korlach, J.; Webb, W. W., Fluorescence correlation spectroscopy with single-molecule sensitivity on cell and model membranes. *Cytometry* **1999,** 36, (3), 176-182.
64. Benes, M.; Billy, D.; Hermens, W. T.; Hof, M., Muscovite (mica) allows the characterisation of supported Bilayers by ellipsometry and confocal fluorescence correlation spectroscopy. *Biological Chemistry* **2002,** 383, (2), 337-341.
65. Koppel, D. E., Statistical accuracy in fluorescence correlation spectroscopy. *Physical Review A* **1974,** 10, (6), 1938-1945.
66. Enderlein, J., Dependence of the optical saturation of fluorescence on rotational diffusion. *Chemical Physics Letters* **2005,** 410, (4-6), 452-456.
67. Dittrich, P. S.; Schwille, P., Photobleaching and stabilization of fluorophores used for single-molecule analysis with one- and two-photon excitation. *Applied Physics B-Lasers and Optics* **2001,** 73, (8), 829-837.
68. Widengren, J.; Rigler, R., Photobleaching investigations of dyes using fluorescence correlation spectroscopy (FCS). *Progress in Biophysics & Molecular Biology* **1996,** 65, PH109-PH109.

69. Patterson, G. H.; Piston, D. W., Photobleaching in two-photon excitation microscopy. *Biophysical Journal* **2000,** 78, (4), 2159-2162.
70. Eggeling, C.; Widengren, J.; Rigler, R.; Seidel, C. A. M., Photobleaching of fluorescent dyes under conditions used for single-molecule detection: Evidence of two-step photolysis. *Analytical Chemistry* **1998,** 70, (13), 2651-2659.
71. Widengren, J.; Rigler, R., Mechanism of photobleaching investigated by fluorescence correlation spectroscopy. *Bioimaging* **1996,** 4, 149-157.
72. Eggeling, C.; Volkmer, A.; Seidel, C. A. M., Molecular photobleaching kinetics of rhodamine 6G by one- and two-photon induced confocal fluorescence microscopy. *Chemphyschem* **2005,** 6, (5), 791-804.
73. de Almeida, R. F. M.; Loura, L. M. S.; Fedorov, A.; Prieto, M., Lipid rafts have different sizes depending on membrane composition: A time-resolved fluorescence resonance energy transfer study. *Journal of Molecular Biology* **2005,** 346, (4), 1109-1120.
74. Loura, L. M. S.; Fedorov, A.; Prieto, M., Fluid-fluid membrane microheterogeneity: A fluorescence resonance energy transfer study. *Biophysical Journal* **2001,** 80, (2), 776-788.
75. Loura, L. M. S.; Fedorov, A.; Prieto, M., Partition of membrane probes in a gel/fluid two-component lipid system: a fluorescence resonance energy transfer study. *Biochimica Et Biophysica Acta-Biomembranes* **2000,** 1467, (1), 101-112.
76. Kahya, N.; Scherfeld, D.; Bacia, K.; Schwille, P., Lipid domain formation and dynamics in giant unilamellar vesicles explored by fluorescence correlation spectroscopy. *Journal of Structural Biology* **2004,** 147, (1), 77-89.
77. Wawrezinieck, L.; Rigneault, H.; Marguet, D.; Lenne, P. F., Fluorescence correlation spectroscopy diffusion laws to probe the submicron cell membrane organization. *Biophysical Journal* **2005,** 89, (6), 4029-4042.
78. Kalb, E.; Tamm, L. K., Incorporation of Cytochrome B5 into Supported Phospholipid-Bilayers by Vesicle Fusion to Supported Monolayers. *Thin Solid Films* **1992,** 210, (1-2), 763-765.
79. Sackmann, E., Supported membranes: Scientific and practical applications. *Science* **1996,** 271, (5245), 43-48.
80. Tamm, L. K., Lateral Diffusion Measurements of Phospholipids in Planar Supported Bilayers and of Antibodies Bound to Supported Bilayers Containing Lipid Hapten. *Biological Chemistry Hoppe-Seyler* **1985,** 366, (9), 859-859.
81. Schutz, G. J.; Schindler, H.; Schmidt, T., Single-molecule microscopy on model membranes reveals anomalous diffusion. *Biophysical Journal* **1997,** 73, (2), 1073-1080.
82. Dimitrov, D. S.; Angelova, M. I., Swelling and Electroswelling of Lipids - Theory and Experiment. *Studia Biophysica* **1986,** 113, (1-2), 15-20.
83. Fagulová, V. Implementation of Time-Resolved Fluorescence Correlation Spectroscopy (TR-FCS) and its Application in the Study of Biomembranes. Diploma thesis, Czech Technical University in Prague, Faculty of Nuclear Sciences and Physical Engineering, Prague, 2006.
84. Schatzel, K.; Drewel, M.; Stimac, S., Photon-Correlation Measurements at Large Lag Times - Improving Statistical Accuracy. *Journal of Modern Optics* **1988,** 35, (4), 711-718.
85. Schatzel, K.; Schulzdubois, E. O., Improvements of Photon-Correlation Techniques. *Infrared Physics* **1991,** 32, 409-416.
86. Magatti, D.; Ferri, F., 25 ns software correlator for photon and fluorescence correlation spectroscopy. *Review of Scientific Instruments* **2003,** 74, (2), 1135-1144.

87. Wahl, M.; Gregor, I.; Patting, M.; Enderlein, J., Fast calculation of fluorescence correlation data with asynchronous time-correlated single-photon counting. *Optics Express* **2003,** 11, (26), 3583-3591.
88. Felekyan, S.; Kuhnemuth, R.; Kudryavtsev, V.; Sandhagen, C.; Becker, W.; Seidel, C. A. M., Full correlation from picoseconds to seconds by time-resolved and time-correlated single photon detection. *Review of Scientific Instruments* **2005,** 76, (8), -
.
89. Wohland, T.; Rigler, R.; Vogel, H., The standard deviation in fluorescence correlation spectroscopy. *Biophysical Journal* **2001,** 80, (6), 2987-2999.
90. Kral, T.; Hof, M.; Jurkiewicz, P.; Langner, M., Fluorescence correlation spectroscopy (FCS) as a tool to study DNA condensation with hexadecyltrimethylammonium bromide (HTAB). *Cellular & Molecular Biology Letters* **2002,** 7, (2), 203-211.
91. Kral, T.; Hof, M.; Langner, M., The effect of spermine on plasmid condensation and dye release observed by fluorescence correlation spectroscopy. *Biological Chemistry* **2002,** 383, (2), 331-335.
92. Kral, T.; Langner, M.; Benes, M.; Baczynska, D.; Ugorski, M.; Hof, M., The application of fluorescence correlation spectroscopy in detecting DNA condensation. *Biophysical Chemistry* **2002,** 95, (2), 135-144.
93. Azoulay, J.; Clamme, J. P.; Darlix, J. L.; Roques, B. P.; Mely, Y., Destabilization of the HIV-1 complementary sequence of TAR by the nucleocapsid protein through activation of conformational fluctuations. *Journal of Molecular Biology* **2003,** 326, (3), 691-700.
94. Huang, Z. P.; Pearce, K. H.; Thompson, N. L., Translational Diffusion of Bovine Prothrombin Fragment 1 Weakly-Bound to Supported Planar Membranes - Measurement by Total Internal-Reflection with Fluorescence Pattern Photobleaching Recovery. *Biophysical Journal* **1994,** 67, (4), 1754-1766.
95. Starr, T. E.; Thompson, N. L., Local diffusion and concentration of IgG near planar membranes: Measurement by total internal reflection with fluorescence correlation spectroscopy. *Journal of Physical Chemistry B* **2002,** 106, (9), 2365-2371.
96. Starr, T. E.; Thompson, N. L., Total internal reflection with fluorescence correlation spectroscopy: Combined surface reaction and solution diffusion. *Biophysical Journal* **2001,** 80, (3), 1575-1584.
97. Hassler, K.; Anhut, T.; Rigler, R.; Gosch, M.; Lasser, T., High count rates with total internal reflection fluorescence correlation spectroscopy. *Biophysical Journal* **2005,** 88, (1), L1-L3.
98. Chance, R. R.; Miller, A. H.; Prock, A.; Silbey, R., Fluorescence and energy transfer near interfaces: The complete and quantitative description of the Eu^{+3}/mirror systems. *Journal of Chemical Physics* **1975,** 63, (4), 1589-1595.
99. Enderlein, J., Single-molecule fluorescence near a metal layer. *Chemical Physics* **1999,** 247, (1), 1-9.
100. Enderlein, J.; Böhmer, M., Influence of interface-dipole interactions on the efficiency of fluorescence light collection near surfaces. *Optics Letters* **2003,** 28, (11), 941-943.
101. Chance, R. R.; Prock, A.; Silbey, R., Comments on the classical theory of energy transfer. *Journal of Chemical Physics* **1975,** 62, (6), 2245-2253.
102. Enderlein, J., Fluorescence detection of single molecules near a solution/glass interface - an electrodynamic analysis. *Chemical Physics Letters* **1999,** 308, (3-4), 263-266.

103. Enderlein, J., A theoretical investigation of single-molecule fluorescence detection on thin metallic layers. *Biophysical Journal* **2000,** 78, (4), 2151-2158.
104. Lambacher, A.; Fromherz, P., Luminescence of dye molecules on oxidized silicon and fluorescence interference contrast microscopy of biomembranes. *Journal of the Optical Society of America B-Optical Physics* **2002,** 19, (6), 1435-1453.
105. Lambacher, A.; Fromherz, P., Fluorescence interference-contrast microscopy on oxidized silicon using a monomolecular dye layer. *Applied Physics a-Materials Science & Processing* **1996,** 63, (3), 207-216.